NEUROSCIENCE

Neural heterogeneity enhances reliable neural information processing: Local sensitivity and globally input-slaved transient dynamics

Shengdun Wu[1], Haiping Huang[2], Shengjun Wang[3], Guozhang Chen[4], Changsong Zhou[5], Dongping Yang[1]*

Cortical neuronal activity varies over time and across repeated trials, yet consistently represents stimulus features. The dynamical mechanism underlying this reliable representation and computation remains elusive. This study uncovers a mechanism for reliable neural information processing, leveraging a biologically plausible network model incorporating neural heterogeneity. First, we investigate neuronal timescale diversity, revealing that it disrupts intrinsic coherent spatiotemporal patterns, induces firing rate heterogeneity, enhances local responsive sensitivity, and aligns network activity closely with input. The system exhibits globally input-slaved transient dynamics, essential for reliable neural information processing. Other neural heterogeneities, such as nonuniform input connections, spike threshold heterogeneity, and network in-degree heterogeneity, play similar roles, highlighting the importance of neural heterogeneity in shaping consistent stimulus representation. This mechanism offers a potentially general framework for understanding neural heterogeneity in reliable computation and informs the design of reservoir computing models endowed with liquid wave reservoirs for neuromorphic computing.

INTRODUCTION

Cortical neurons exhibit substantial spiking time irregularity and trial-to-trial variability in both spontaneous activities and evoked responses to repeated stimuli (*1*, *2*). Despite this notable variability, neural representations of stimuli remain functionally consistent (*3*–*6*). Stimulus onset widely quenches neural variability (*7*) and leads to reliable sensory coding (*6*). Neural population dynamics has been suggested to straightforwardly produce resilient movement patterns, even when confronted with highly unpredictable neural responses (*8*, *9*). Thus, a central challenge is to understand the neural mechanisms that reconcile inherent cortical variability with reliable representations of external inputs.

Randomly connected recurrent neural networks (RNNs) with excitation-inhibition (E-I) balance (*10*) are often used to model irregular and asynchronous activity with reliable macroscopic dynamics, but they mainly track low-dimensional inputs (*8*, *10*, *11*). Spatially extended spiking neural networks (SNNs), incorporating the distance-dependent connection probability (*12*), limit dynamical complexity but can also generate intricate spatiotemporal dynamics through Turing-Hopf bifurcation, producing coherent spatiotemporal patterns (*13*, *14*). These destabilized networks can be used for reservoir computing (*15*), whose reliability can be achieved by breaking the symmetry of network dynamics via nonuniform input connections (*13*), referred to as neural heterogeneity in terms of heterogeneous input connections. This suggests that neural heterogeneity essentially contributes to neural computation, as previously demonstrated, e.g., through the heterogeneity of cell spiking thresholds (*16*) or membrane time constants (*17*). However, the underlying dynamical mechanism remains elusive.

Biological neural populations are highly heterogeneous, varying in structure, gene expression, and electrophysiological properties, such as membrane capacitance and resistance, resting potential, or spiking threshold. These variations capture the difference in the structural composition of the cell membrane across neurons of both the same and distinct types (*18*–*20*). Emerging research suggests that neuronal diversity plays a pivotal role in information processing (*16*, *17*, *21*–*23*). Excitability heterogeneity serves as a homeostatic control mechanism that enriches neural dynamics and enhances network resilience by stabilizing responses to modulatory input and preserving robust brain function (*22*). This heterogeneity in cell spiking thresholds further enables computational specialization in brain circuits by differentially regulating the gating, encoding, and decoding of signals in E and I neurons, in turn expanding the functional repertoire of local networks (*16*). On the other hand, neuronal heterogeneity in terms of membrane and synaptic time constants [observed in the brain (*18*–*20*)] enhances robust learning (*17*). Furthermore, a reservoir computing model with diverse timescales achieves superior prediction accuracy and flexibility for multiscale chaotic dynamics by dynamically selecting appropriate timescales, outperforming standard reservoir computing models with identical neurons in both short- and long-term forecasting tasks (*23*). However, despite these advances, a dynamical mechanism to understand the reliability of input representation and computation remains absent, and a unified framework to elucidate the roles of various neural heterogeneities has yet to be established.

Here, we reveal a potentially general dynamical mechanism, starting by investigating two specific neural diversities: heterogeneous leakage time constants and gain time constants (*18*, *24*). We explore their roles in the reliability of computation regarding an input-output mapping task, using a biologically plausible SNN model. Our findings show that either diversity can enhance reliable computation, playing a role similar to that of nonuniform input

[1]Research Centre for Frontier Fundamental Studies, Zhejiang Lab, Hangzhou 311100, China. [2]PMI Lab, School of Physics, Sun Yat-sen University, Guangzhou 510275, China. [3]Department of Physics, Shaanxi Normal University, Xi'an 710119, China. [4]National Key Laboratory for Multimedia Information Processing, School of Computer Science, Peking University, Beijing, China. [5]Department of Physics, Hong Kong Baptist University, Kowloon Tong, Hong Kong, China.
*Corresponding author. Email: dpyang@zhejianglab.com

connections (*13*). It suggests a unique dynamical mechanism, relying on consistent representation: The diversity disrupts intrinsic coherent spatiotemporal patterns (*13*, *25*) and induces firing rate heterogeneity, leading to local sensitivity and globally input-slaved transient dynamics (*26*). This dynamics shapes the high-dimensional representation, inducing a liquid-like spatiotemporal activity pattern and forming input-slaved trajectories for reliably representing input information (*26*). This mechanism is robust across networks with varying connection ranges and connectivity randomness, and explains the similar roles of other heterogeneities, such as nonuniform input connections, spike threshold heterogeneity, and network in-degree heterogeneity. It provides a potentially uniform framework for understanding the significance of various forms of neural heterogeneities in ensuring reliable neural information processing. Thus, our work sheds light on reservoir computing models endowed with this mechanism.

RESULTS

To investigate the dynamical mechanism underlying reliable computation, we start by exploring the effect of neuronal timescale diversity on spatiotemporal activity properties, leveraging the spatially extended E-I SNNs with current-based leaky integrate-and-fire (LIF) neurons (Fig. 1A). We show that neuronal timescale diversity can lead to robust and reliable computation and representation with no need of fine-tuning connection ranges and special spatial topology. The dynamical mechanism is presented and comprehended from three perspectives: local responsive sensitivity, input-induced global spatiotemporal modes, and high-dimensional transient dynamics, ensuring robust and reliable representation and computation. In addition, we show that neuronal timescale diversity expands representation space in the asynchronous state, explaining why homogeneous balanced networks fail to track chaotic time series. This mechanism also explains similar roles of other neural heterogeneities, such as nonuniform input connections, spike threshold heterogeneity, and network in-degree heterogeneity, demonstrating a potentially general framework for understanding the role of neural heterogeneity in ensuring reliable neural information processing.

Neuronal timescale diversity and its impact on spatiotemporal dynamics: A model-based analysis

We commence by illustrating in Fig. 1A the spatially extended E-I SNN with distance-dependent connection probabilities (*13*, *27*). The connectivity profiles can be characterized by connection ranges

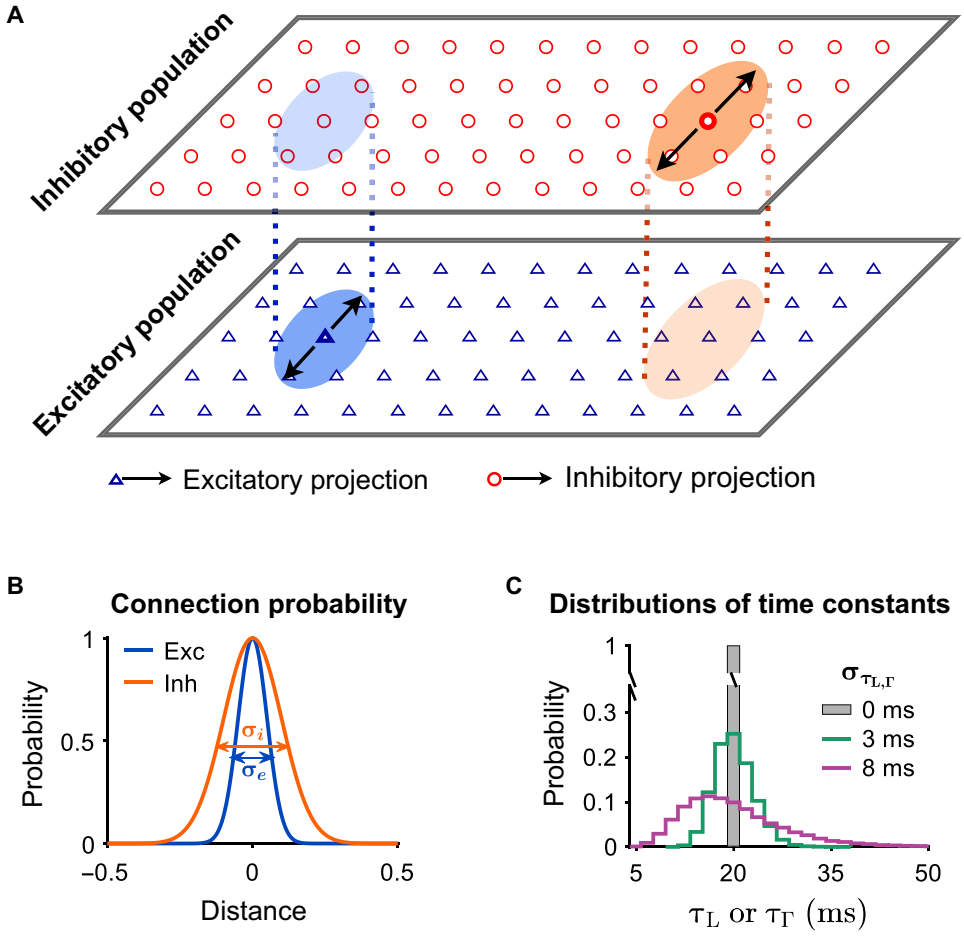

Fig. 1. Schematic of spatially extended SNNs with diversity of two time constants in neuronal dynamics. (**A**) Network architecture. Excitatory (E, blue) and inhibitory (I, orange) neurons evenly distribute on a two-dimensional (2D) plane: [0, 1] × [0, 1]. (**B**) They are connected with a distance-dependent Gaussian probability, characterized by connection ranges σ_e and σ_i for E and I neurons, respectively. By default, $\sigma_e = 0.05$ and $\sigma_i = 0.1$, except in cases where specific conditions or parameters warrant adjustments. (**C**) Distributions of time constants τ_L and τ_Γ with widths $\sigma_{\tau_{L,\Gamma}} = 0$ ms (gray), 3 ms (green), and 8 ms (purple).

σ_e and σ_i for E and I neurons (Fig. 1B), respectively. Two distinct types of neuronal time constants are considered in the LIF neuron model: The leakage time constant τ_L controls the decay rate of the neuron's membrane potential; the gain time constant τ_Γ regulates the overall scale of network drives (*18*, *24*). We investigate scenarios where τ_L and τ_Γ exhibit individual or joint diversities, as evidenced in biological datasets (*18*, *24*). As the timescale is nonnegative, the diversity is introduced with simple lognormal distributions, akin to those measured in experimental data (*19*, *20*), and characterized by distribution widths σ_{τ_L} and σ_{τ_Γ} for τ_L and τ_Γ (Fig. 1C), respectively. The parameter ρ controls the shared proportion of their distributions. When τ_L and τ_Γ are completely correlated ($\rho = 1$), both are equal to the membrane time constant τ_m, and the neuronal model becomes equivalent to that used in (*17*). For more details, refer to Materials and Methods.

In the homogeneous network ($\sigma_{\tau_L} = 0$), broader recurrent inhibition ($\sigma_i > 2\sigma_e$) can lead to pattern formation through a Turing-Hopf bifurcation: breaking the spatiotemporal symmetry (fig. S1A). This gives rise to a remarkably coherent spatiotemporal pattern of collective activities of E neurons, wherein local E populations exhibit synchronized oscillations and spiking activity is irregular (Fig. 2A). In the local sites, synchronized oscillations are also evidenced by the sharp peaks in the power spectrum (Fig. 2B) and strong pairwise synchrony (Fig. 2C), as well as the broad distribution of pairwise spike count correlation (Fig. 2D). It spatially destabilizes the local E-I balance (fig. S2), leading to pronounced temporal fluctuations in firing rates ($\sigma_{\tau_L} = 0$ in Fig. 2E). This can be understood by mean-field analysis under a diffusion approximation (*27*) with the ansatz of the Gaussian distribution of firing rates (Fig. 2F) (*13*).

Now, we investigate the effects of τ_L diversity on network dynamics (Fig. 2). Increasing τ_L diversity gradually disrupts Turing-Hopf bifurcation (*13*, *25*), leading to a decrease in temporal rate fluctuations (Fig. 2E). The decrease indicates a suppression of the coherent spatiotemporal patterns characteristic of the Turing-Hopf bifurcation regime in the homogeneous network ($\tau_L = 0$). In the heterogeneous network, neurons exhibit much weaker oscillations and local synchronization (Fig. 2A), leading to much weaker average oscillatory amplitudes with a broader frequency distribution (Fig. 2B), substantially lower pairwise synchrony (Fig. 2C), and spike count correlation (Fig. 2D). Thus, this heterogeneity disrupts the local synchronization required to sustain the coherent patterns. The reduction in synchronized activity leads to E-I rebalance (fig. S2) in the

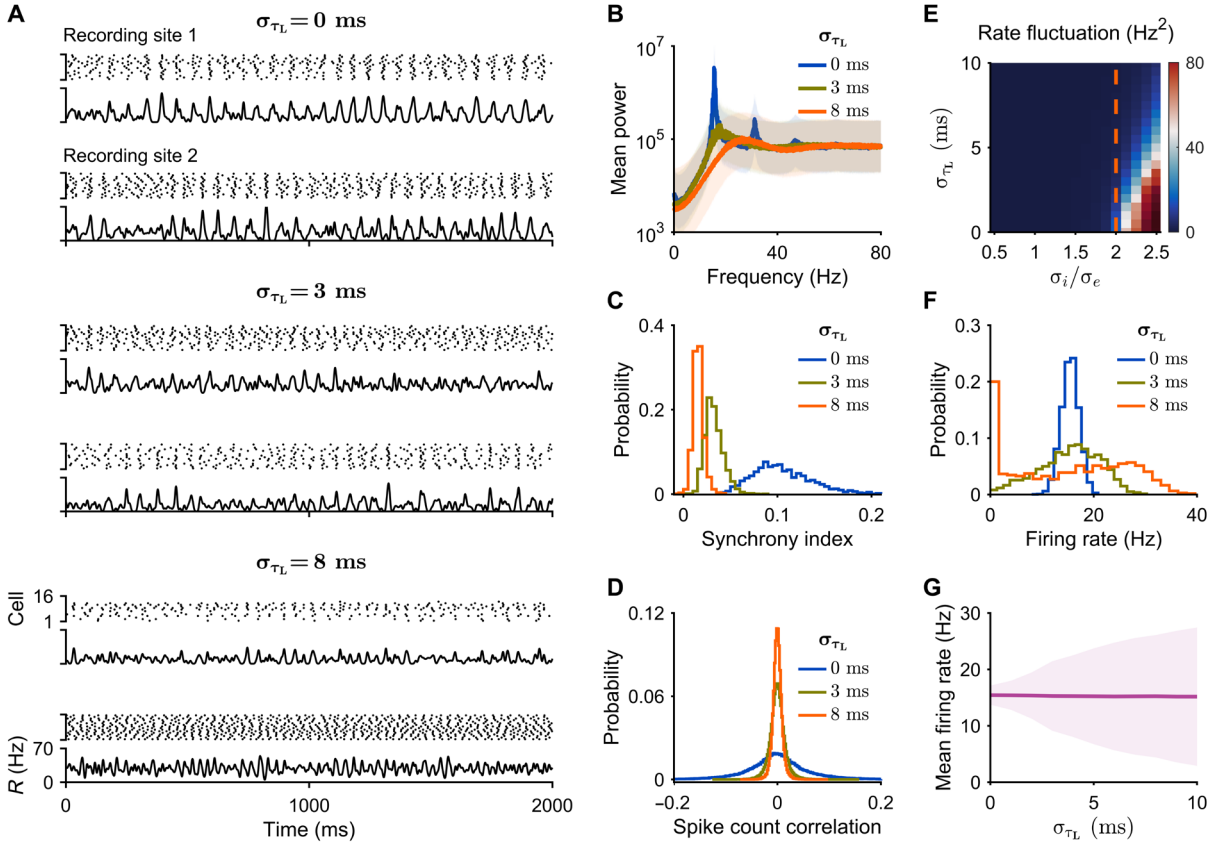

Fig. 2. Spontaneous spatiotemporal dynamics in networks with or without timescale diversity. We record the activity of 2500 spatial sites with each one comprising 16 E neurons. Neurons within each site have identical timescales, but the timescales vary across different sites, introducing diversity. (**A**) Raster plot and firing rate series of two randomly chosen sites in the homogeneous network ($\sigma_{\tau_L} = 0$ ms, top) and the heterogeneous network ($\sigma_{\tau_L} = 3$ ms, middle, and $\sigma_{\tau_L} = 8$ ms, bottom). (**B**) Average power spectra (thick lines) of individuals' firing rates with shaded areas denoting SDs. (**C**) Synchrony index distributions. (**D**) Distributions of pairwise spike count correlations. (**E**) Mean temporal fluctuations of E neurons' firing rates across the parameter space (σ_{τ_L}, σ_i / σ_e), where the dashed line represents the critical value of σ_i / σ_e for Turing-Hopf bifurcation in the homogeneous network ($\tau_L = 0$). The value is averaged over all spatial sites. (**F**) Firing rate distributions of E neurons. (**G**) Mean firing rates (thick line) and their SDs (shaded area) plotted against σ_{τ_L}.

neurons, resulting in more irregular and desynchronized firing (Fig. 2A) and a more robust asynchronous state (*11*).

The interplay between local E-I balance and time constant diversity plays a crucial role in stabilizing the asynchronous state. The E-I balance ensures that the excitation and inhibition in the local site are balanced, preventing runaway excitation or excessive inhibition. When combined with τ_L diversity, the heterogeneity further dampens any residual synchrony, enhancing the network's ability to maintain irregular, uncorrelated firing patterns (Fig. 2, C and D). Thus, increasing τ_L diversity reduces temporal rate fluctuations by disrupting the coherent spatiotemporal patterns (fig. S1, B and C), supporting a robust asynchronous state characterized by irregular, desynchronized neuronal activity. This state is conducive to reliable information processing, as it prevents the dominance of intrinsic coherent patterns that could interfere with the representation of external inputs.

With τ_L diversity, neuronal firing rates exhibit a broader non-Gaussian distribution (Fig. 2F): a weighted summation of timescale-dependent Gaussian distributions (fig. S3), thus complicating the mean-field analysis. Nonetheless, it can be understood via a simplified model of diffusively coupled nonlinear oscillators, where timescale diversity has been proved to stabilize the asynchronous state and prevent interaction-induced coherence (*28*–*30*). Specifically, a larger σ_{τ_L} induces a larger heterogeneity of site firing rates with more sites at a low activity level, while its overall average remains stable (Fig. 2G). This spatial heterogeneity in neuronal activity is consistent with experimental records showing considerable variability in firing rates across neurons (*31*).

Similar effects of τ_Γ diversity on network dynamics are presented in fig. S4. With either timescale diversity, neurons' linear response functions behave spatially heterogeneous, and thus, their diversities can disrupt intrinsic coherent spatiotemporal patterns. These stabilized network dynamics are expected to support reliable computation.

Enhancing reliability in input-output computation and Mackey-Glass signal representation via timescale diversity

We now examine the role of timescale diversity in reliable computation regarding input-output mapping in a reservoir computing setting (Fig. 3A). Reservoir computing is particularly suited for tasks with temporal data, using a fixed, high-dimensional dynamical system (the "reservoir") to process input signals. This framework allows complex temporal patterns into spatiotemporal representations within the reservoir, facilitating easier decoding and analysis through simple readout mechanisms. Using a reservoir composed of spiking neurons with diverse timescales, we can explore how timescale diversity influences reliable computation and input-output mapping. This approach helps us understand complex spatiotemporal dynamics and assess the network's ability to handle temporal inputs. Analyzing the network's responses shows how timescale diversity enhances its capacity for processing complex patterns and performing reliable computations.

In this task, we aim to assess the network's ability to perform reliable input-output mapping when processing complex temporal patterns within a reservoir computing framework (Fig. 3A). The network is driven by a sinusoidal input signal: $I_{\sin} = \epsilon \cdot \sin(2\pi f_{\sin} t)$, where ϵ is its amplitude and $f_{\sin}$ is its frequency. The readout layer, which consists of local rate readouts from the reservoir, is trained to produce an output signal that is a composite of three sinusoidal components: $I_{\text{target}} = 1.5 \cdot [\sin(\pi f_{\sin} t) + \sin(2\pi f_{\sin} t) - \sin(3\pi f_{\sin} t)]$. This composite target includes the following: (i) fundamental component matching the frequency $f_{\sin}$, (ii) subharmonic component with a lower frequency introducing slower oscillations and adding complexity, and (iii) nonharmonic component with a frequency not directly related to the fundamental frequency $f_{\sin}$ and thus introducing additional challenge.

The readout weights are trained using a ridge least square method (LSM) to map the reservoir's activity to the target time series (Fig. 3, B and C). In the homogeneous network ($\tau_{L,\Gamma} = 0$), the outputs poorly

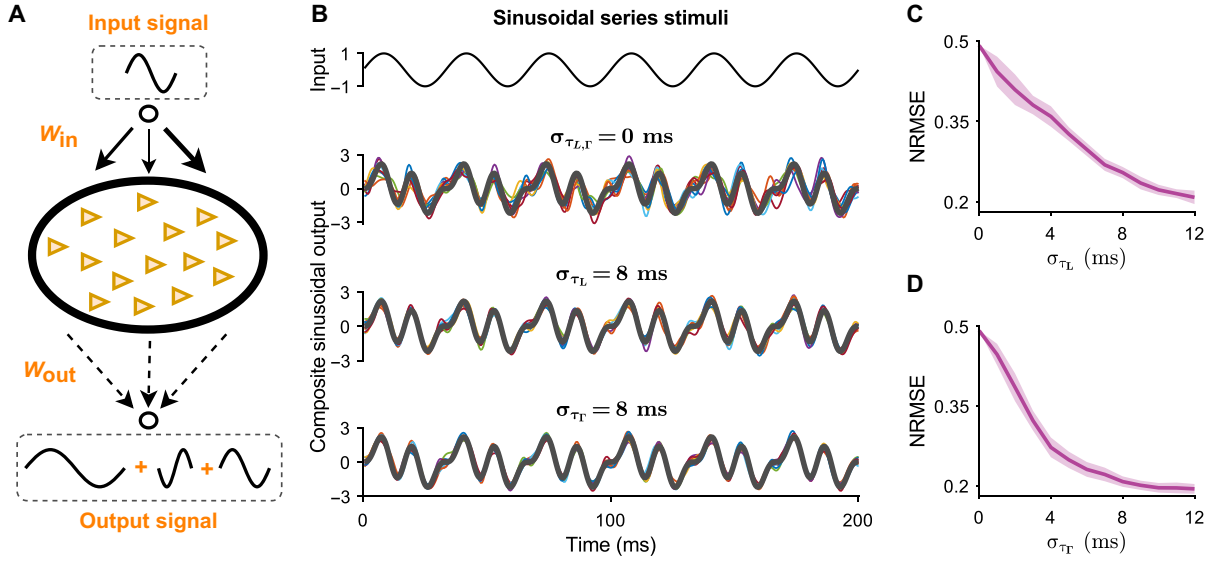

Fig. 3. Enhanced reliability of computation. (**A**) Schematic of the input-output mapping task. (**B**) Time trace of the input (top) and computations from the homogeneous network ($\sigma_{\tau_{L,\Gamma}} = 0$ ms, second layer) and the heterogeneous networks with leakage timescale diversity ($\sigma_{\tau_L} = 8$ ms, third layer) or gain timescale diversity ($\sigma_{\tau_\Gamma} = 8$ ms, bottom). The black line represents the target signal, and the overlapped colored lines depict the outputs from 10 repeated trials. (**C** and **D**) Target fitting normalized root mean square error (NRMSE) plotted against σ_{τ_L} (C) and σ_{τ_Γ} (D). Parameter setting: amplitude $\epsilon = 30$ mV and frequency $f_{\sin} = 30$ Hz.

track the target time series and display noticeable variability across trials (Fig. 3C), indicating unreliable computation. In contrast, introducing diversity in τ_L or τ_Γ enables the network to produce outputs that closely match the target signal consistently across trials (Fig. 3C). These results demonstrate that both τ_L and τ_Γ diversities enhance the network's computation reliability. Specifically, larger σ_{τ_L} or σ_{τ_Γ} leads to lower normalized root mean square error (NRMSE) across multiple trials (Fig. 3, D and E), indicating a reduced trial-to-trial variability and improved performance.

This reliable computation in heterogeneous networks reminds us of a reliable information representation. To examine this, we repeatedly apply a segment of one-dimensional (1D) Mackey-Glass (MG) chaotic series (*32*) to the networks and use the LSM method to reconstruct the input from neural response activities (Fig. 4A). The MG signal is characterized by its intrinsic pace f_{MG} (*32*), which showcases a distinct frequency range. Because the MG signal has a high-dimensional chaotic attractor in phase space, successfully representing it requires a rich repertoire of network dynamical states (see note S1 for details).

As depicted in Fig. 4B, the reconstructed MG output signals from 10 repeated trials (overlapping colored lines) closely follow the trend of the MG input signal (black line) but exhibit various degrees of variability across trials. For the homogeneous network ($\sigma_{\tau_L} = 0$ ms), the outputs show considerable trial-to-trial variability and are short of accuracy in tracking input signals (Fig. 4B). Conversely, for heterogeneous networks with intermediate and high degrees of timescale diversity ($\sigma_{\tau_L} = 3$ and 8 ms), output signals display substantially reduced trial-to-trial variability (Fig. 4B). Various MG series with different paces, $f_{MG} = 20, 50,$ and 110, can be reliably represented in the heterogeneous network activity (Fig. 4C), with a slightly higher NRMSE for the fast-changing MG signal ($f_{MG} = 110$). Furthermore, these timescale diversities also enhance the reliability of MG signal prediction (fig. S5).

The representation reliability is robust against various connection range ratios σ_i / σ_e (Fig. 4D). For homogeneous networks ($\sigma_{\tau_L} = 0$ ms) or networks with a low level of timescale diversity ($\sigma_{\tau_L} = 3$ ms), NRMSE initially decreases with increasing σ_i / σ_e, reaching a minimum before rising again (Fig. 4D, left). It is due to stabilized rich activity patterns near the critical point ($\sigma_i / \sigma_e \approx 2$) (*13*). As presented in Fig. 2C, the critical point shifts to a larger ratio when timescale diversity is increased. Thus, the ratio at which the minimal NRMSE occurs also shifts to a larger value with increasing timescale diversity. Notably, for heterogeneous networks with $\sigma_{\tau_L} = 8$ ms, NRMSE remains stable at considerably low values across a wide range of σ_i / σ_e, demonstrating robustness against σ_i / σ_e, as network dynamics remain stable across a broad range of σ_i / σ_e (Fig. 2C). Even in networks with connections randomly shuffled, both timescale diversities consistently enhance reliable representation (fig. S6). It indicates that the distance-dependent spatial topology is not substantial in the heterogeneous network.

Similar results are obtained for σ_{τ_Γ} (Fig. 4, C and D, right), demonstrating that timescale diversity essentially enhances reliable representation and computation. Note that the network achieves a lower NRMSE in the MG signal reconstruction task (Fig. 4) than in the input-output mapping task with the sinusoidal input (Fig. 3). The MG signal reconstruction involves mapping a complex but directly correlated input signal to the output without generating new frequencies. In contrast, while the sinusoidal input is simpler, the target output is a composite signal that includes subharmonic and nonharmonic components not present in the input. This means that the network must generate additional frequencies from the input, which is more challenging than directly reconstructing the MG signal input in the output.

These results underscore the substantial role of timescale diversity in enhancing reliable representation and computation through a mechanism that differs from the reliance on spatially coherent

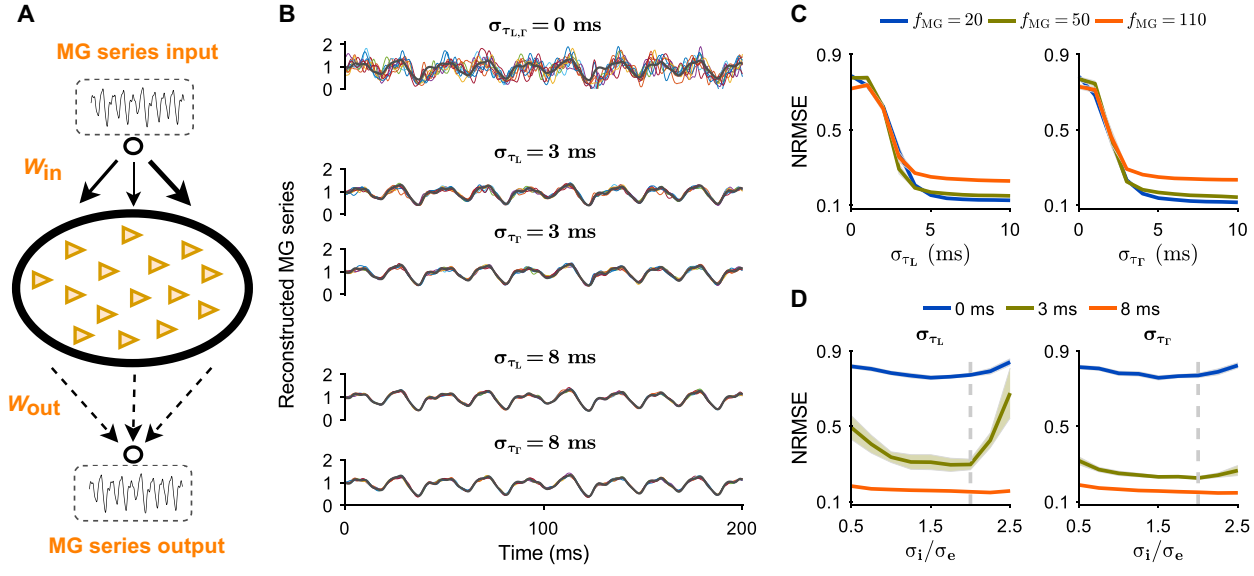

Fig. 4. Enhanced reliability of MG signal reconstruction by timescale diversity. (**A**) Task illustration. (**B**) MG signals reconstructed MG series from networks with σ_{τ_L} (or σ_{τ_Γ}) = 0 ms (top), 3 ms (middle), or 8 ms (bottom). Line colors denote the same as those in Fig. 3B. (**C**) NRMSE plotted against σ_{τ_L} (left) and σ_{τ_Γ} (right) at $f_{MG} = 20$, 50, or 110. (**D**) NRMSE plotted against the ratio σ_i / σ_e at σ_{τ_L} (or σ_{τ_Γ}) = 0, 3, and 8 ms, where the dashed line represents the critical value of σ_i / σ_e for Turing-Hopf bifurcation in the homogeneous network ($\tau_L = 0$). Shaded areas represent SDs. In (B) and (D), $f_{MG} = 50$.

intrinsic patterns in overcoming the difficulty of reservoir computing with spiking networks (*13*). Its robustness informs a unique underlying dynamical mechanism supporting the reliability of input representation and computation.

A potentially general dynamical mechanism for reliable representation and computation

The dynamical mechanism found here can be unfolded as the following three perspectives: local responsive sensitivity, input-induced global spatiotemporal modes, and high-dimensional transient trajectories. We start by presenting the mechanism in the default condition $\sigma_e \equiv 0.05$ and $\sigma_i \equiv 0.1$ and then apply this mechanism in the other condition with $\sigma_i / \sigma_e \equiv 0.5$.

Timescale diversity enhancing local responsive sensitivity

We first show how timescale diversity affects the network's response to external stimuli. We apply small-amplitude sinusoidal periodic signals to the networks and examine the local site-responsive properties (Fig. 5A). Both homogeneous and heterogeneous networks exhibit a response power peak at the stimulus frequency, e.g., $f_{sin} = 10$ or 30 Hz (Fig. 5B). The network with a larger heterogeneity shows a higher response amplitude, indicating superior sensitivity to the periodic stimuli (see Materials and Methods).

The enhanced sensitivity can be attributed to three factors arising from timescale diversity. First, it disrupts the intrinsic coherent spatiotemporal patterns (Fig. 2A and fig. S1) (*13*, *25*), liberating site activity to be more sensitive. Second, the disruption allows the local E-I balance to recover (fig. S2), further increasing the sensitivity of site activity. Last, this disruption induces spatial firing rate heterogeneity with more sites exhibiting low activity levels (Fig. 2F), which are most sensitive (fig. S7, A to D). Therefore, timescale diversity renders site activity more sensitive, with more sites effectively responding to the input (the regions with sensitivity > 1 in Fig. 5C). Consequently, with more effective responses, the input more strongly influences the network activity, resulting in a higher average signal-to-noise ratio (SNR; see Materials and Methods), which substantially increases with σ_{τ_L} (Fig. 5, D and E). In this way, timescale diversity improves the effectiveness of the network's response to external stimuli.

Furthermore, the sensitivity property explains why the correlation ρ between these two timescales impedes the beneficial effects of timescale diversity on the reliability of computation. The leaky timescale τ_L, when larger, implies slower leakage and easier firing, leading to a higher firing rate (fig. S7A). In contrast, a higher value of τ_Γ indicates that the neuron requires more time to assimilate the driving current, making it more difficult to fire and resulting in a lower firing rate (fig. S7B). In general, the highest sensitivity is achieved when the site exhibits low activity levels, e.g., when sites' firing rates are just above zero (fig. S7, C and D). Thus, site responsiveness depends differently on τ_L and τ_Γ (Fig. 6, A and B, left), with highly sensitive sites observed at small τ_L or large τ_Γ. This mismatch leads to a distinct distribution of highly sensitive sites across the 2D space of different heterogeneous networks with τ_L or τ_Γ diversity (Fig. 6C). Consequently, when they are uncorrelated (e.g., the correlation ρ is low), site sensitivities due to individual timescale diversity can be preserved and the number of site sensitivities is maximized. On the other hand, increasing their correlation ρ reduces site sensitivity and the number of highly sensitive sites (Fig. 6, D and E). Moreover, with the reduced site sensitivity, the benefits of individual timescale diversity diminish, causing the spatiotemporal patterns to revert to those seen in homogeneous networks (fig. S8). Because SNR is positively

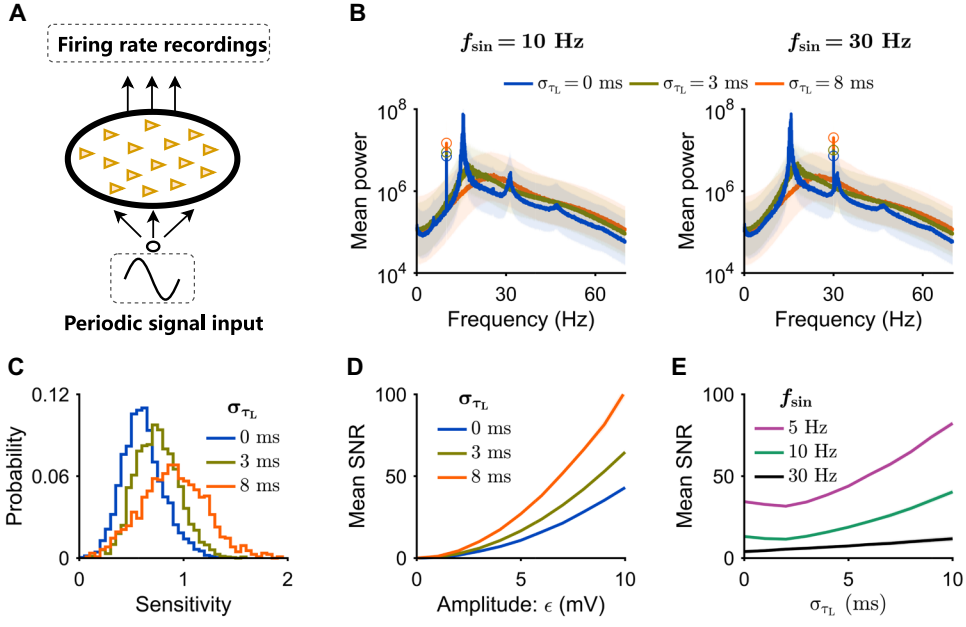

Fig. 5. Timescale diversity enhances network responsive sensitivity. (**A**) Schematic representation of the network receiving a sinusoidal input. (**B**) Averaged power spectrum of evoked firing rates for homogeneous ($\sigma_{\tau_L} = 0$ ms, blue) and heterogeneous ($\sigma_{\tau_L} = 3$ ms, green, and $\sigma_{\tau_L} = 8$ ms, orange) networks. The value is averaged over all spatial sites, with SDs represented by shaded areas. Circular markers denote the peak power spectral density of the network's response to sinusoidal periodic stimuli with an amplitude $\epsilon = 3$ mV at $f_{sin} = 10$ Hz (left) or 30 Hz (right). (**C**) Distributions of site-responsive sensitivities, as defined in Materials and Methods. (**D**) Mean signal-to-noise ratio (SNR) plotted against stimulus amplitude ϵ. (**E**) Mean SNR plotted against σ_{τ_L} for sinusoidal stimuli at $f_{sin} = 5$, 10, or 30 Hz. In (D) and (E), SDs over trials are so small that the shaded areas are covered by lines.

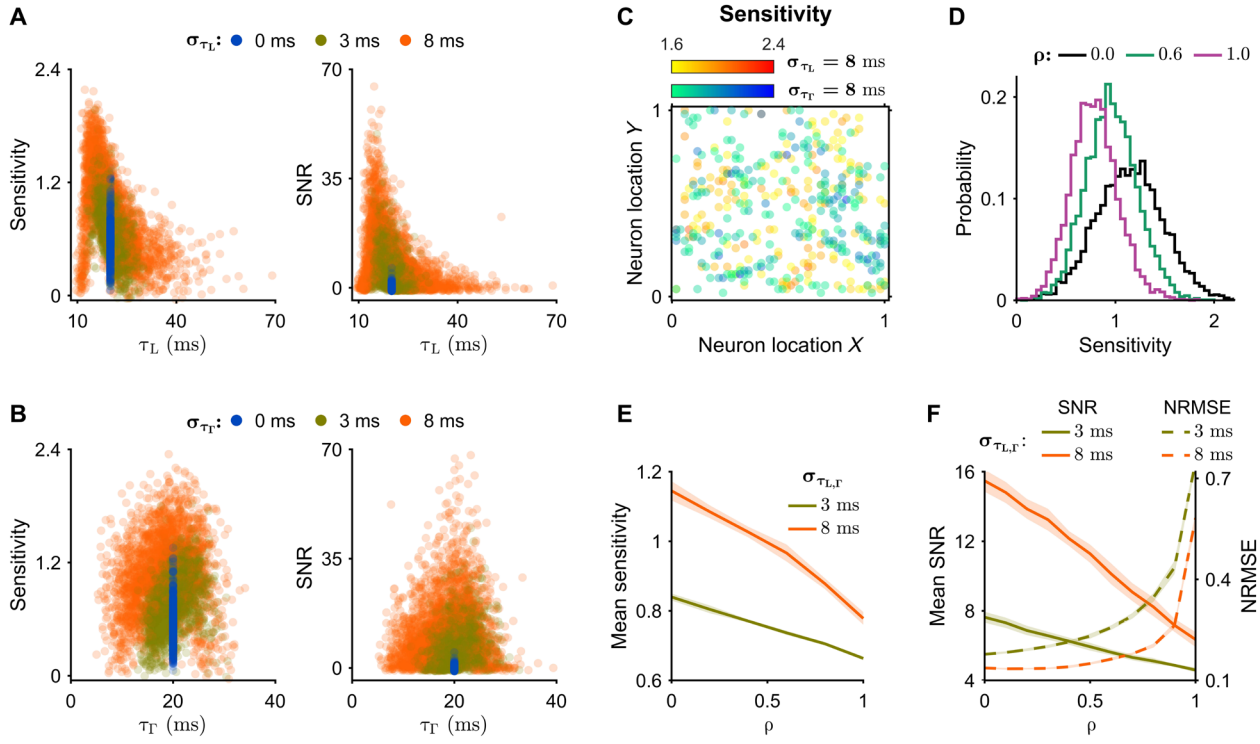

Fig. 6. Correlation between leakage and gain timescales impedes the beneficial effects of timescale diversity on computation's reliability. (**A**) Responsive sensitivities (left) and SNRs (right) plotted against τ_L at each site. (**B**) Similar to (A) but for τ_Γ. (**C**) Spatially distributed site-responsive sensitivities (for all sites with sensitivity > 1.6). Red or blue dots represent the recording sites in networks with $\sigma_{\tau_L} = 8$ ms or $\sigma_{\tau_\Gamma} = 8$ ms, respectively. Darker colors indicate higher sensitivity values. (**D**) Distributions of site-responsive sensitivities at various ρ. (**E**) Mean sensitivity (D) plotted against ρ. (**F**) Mean SNR and NRMSE plotted against ρ. In (E) and (F), the value is averaged over trials, with SDs represented by shaded areas. For calculating sensitivity and SNR in all panels, the frequency and amplitude of the sinusoidal input are $f_{sin} = 30$ Hz and $\epsilon = 3$ mV, respectively. For calculating NRMSE in (F), the input is the MG signal with $f_{MG} = 50$.

correlated with sensitivity (fig. S7, E and F), the input signal is best encoded in sites with different values of τ_L and τ_Γ (Fig. 6, A and B, right). As a result, the mean SNR decreases as the correlation between these two timescales increases (Fig. 6F), subsequently impairing the network's computational performance (Fig. 6F).

These results demonstrate that while timescale diversity introduces spatial heterogeneity in network activity, it enhances the network's responsiveness to external signals. This suggests that the dynamics in networks with timescale diversity are better suited to incorporate the input information, ultimately benefiting representation and computation.

Timescale diversity shaping consistent stimulus representation

With timescale diversity, a substantial number of sensitive sites are distributed across the network, enabling more neurons to be effectively responsive to the input. These sensitive neurons react robustly when activated by the input, and their activities propagate through the network, interacting with one another. This collective behavior can eventually lead to the emergence of an input-related coherent spatiotemporal wave or flowing mode. Consequently, the presence of these distributed sensitive sites facilitates sufficient neuronal activation to generate stable, coherent input-driven modes, enhancing reliable representation and computation.

To demonstrate this speculation, we use the data-driven dynamic mode decomposition (DMD) method (*33*) to analyze how networks represent external inputs through spatiotemporal patterns and how timescale diversity shapes this representation (Fig. 7A). DMD decomposes complex, high-dimensional neural activities into modes with specific spatial and temporal characteristics (Fig. 7A). In general, when the network is driven by an input, its intrinsic spatiotemporal dynamics are perturbed, leading to a competition between intrinsic dynamical modes and input-induced ones. To illustrate this competition, we examine both spontaneous and input-induced spatiotemporal activity patterns (Fig. 7, B and D). By comparing their DMD modes, we investigate how these spatiotemporal dynamics represent input information and the role of neural heterogeneity in this process.

We demonstrate the role of timescale diversity in shaping consistent stimulus representation by examining the eigenvalue spectra of DMD modes (Materials and Methods). Consistent with the Turing-Hopf bifurcation in the homogeneous network ($\sigma_{\tau_L} = 0$ ms), its spontaneous activities show strong intrinsic dynamical modes (Fig. 7B, left). Applying the MG series to the network suppresses its intrinsic modes without inducing a new mode (Fig. 7C, left). This indicates that the homogeneous network cannot generate spatiotemporal patterns that effectively encode the input signal because its site activity exhibits low sensitivity and SNR (Fig. 5) and thus lacks the input information. In addition, without enough highly sensitive sites, the input-induced activities are hard to propagate out consistently and support the generation of an input-related spatiotemporal mode. In contrast, in the heterogeneous network ($\sigma_{\tau_L} = 8$ ms), timescale diversity disrupts the intrinsic dynamical modes (*13*, *25*), leaving only one stationary pattern (Fig. 7B, right), which is the network-wide

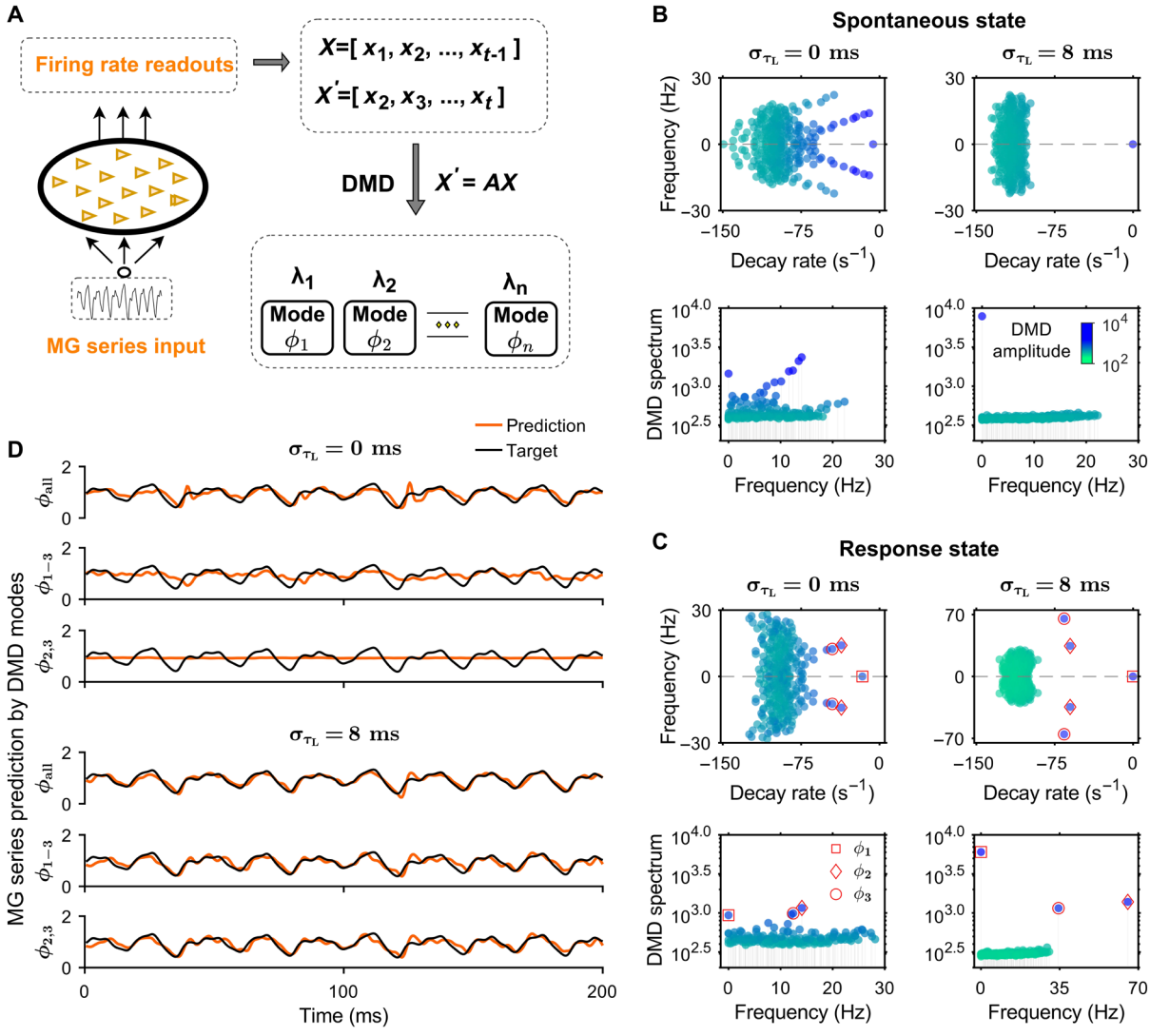

Fig. 7. DMD for characterizing spatiotemporal patterns of neural activities. (**A**) Schematic of the network receiving MG series input and DMD analysis procedure. (**B**) DMD eigenvalue spectrum for spontaneous network activities in homogeneous ($\sigma_{\tau_L} = 0$ ms, left) or heterogeneous ($\sigma_{\tau_L} = 8$ ms, right) networks. Top: DMD eigenvalues λ in the complex plane of the decay rate $\sigma = \mathrm{Re}(\ln\lambda_k) \cdot dt^{-1}$ and the frequency $f = \mathrm{Im}(\ln\lambda_k) \cdot (2\pi \cdot dt)^{-1}$ with time resolution $dt = 1$ ms. Bottom: Mode amplitudes (dot colors) plotted against frequencies. (**C**) Similar to (B), but for network activities in response to MG series input. The red square, diamond, and circular markers denote the first three dominant DMD modes, respectively. (**D**) DMD modes extracted for MG series prediction at four time steps ahead in homogeneous ($\sigma_{\tau_L} = 0$ ms, top) or heterogeneous ($\sigma_{\tau_L} = 8$ ms, bottom) networks. Predicted MG output signals from all modes ϕ_{all}, three dominant DMD modes ϕ_{1-3}, and select modes $\phi_{2,3}$. In the heterogeneous network ($\sigma_{\tau_L} = 8$ ms, bottom), DMD analysis identifies two new input-induced modes ($\phi_{2,3}$) in the right panels.

baseline response to the external input. The input drives this network to induce two new dynamical modes (red circled and diamonded in Fig. 7C, right), which are closely associated with the input dynamics (positioned within the MG frequency range in this case) and thus may be sufficient to encode the input effectively. Note that similar results can be obtained in the spatiotemporal dynamics induced by various types of input signals (e.g., the signal from the Lorentz system as demonstrated in fig. S9), not just those with oscillatory components.

Our analysis shows that neural heterogeneity disrupts the internal spatiotemporal patterns, enabling the input to induce new, input-related spatiotemporal modes (red circled or diamonded in Fig. 7C, right). These new modes lead to reliable representation of the input, despite intrinsic dynamics and variability across trials. Therefore, DMD analysis provides insights into how neural heterogeneity influences the temporal and spatial patterns of network activity, highlighting the emergence of input-induced modes that improve reliability.

We further check whether the input-induced dynamical modes are enough to represent the external input in the heterogeneous network. We use all modes ϕ_{all}, three dominant ones ϕ_{1-3}, or the only two new input-induced ones $\phi_{2,3}$ to predict the system's short-term future states (four time steps ahead) (Fig. 7D). The output weights are linearly regressed to reconstruct the MG input signal for predicting its future states. The result confirms that the three dominant modes contain enough information about the input to fulfill this task, whose performance is comparable with that using all modes.

Notably, the two input-induced modes achieve a similar performance with those using all modes or three dominant ones, indicating that the first mode ϕ_1 contributes little to the computation and the two input-induced modes contain enough information about the input. In contrast, in the homogeneous network, even with all modes, it is unavailable to precisely predict the MG signal's future states, indicating that the network fails to capture the key features of the input (Fig. 7D).

These results show that because the heterogeneous network is far from the Turing-Hopf bifurcation and lacks intrinsic coherence (Fig. 2C), it effectively responds to external stimuli and captures the features of stimulus signals. It demonstrates that timescale diversity shapes consistent stimulus representation by inducing input-related dynamical modes, because of its firing rate heterogeneity and locally enhanced sensitivity to external inputs with high SNR. Therefore, it is beneficial for reliable representation and computation.

Timescale diversity reducing high-dimensional trial-to-trial variability

We further explore how the input is represented in the network's activity space by applying principal components analysis (PCA) to the local rates. PCA allows us to explore the structure of population response activities and understand how neural heterogeneity affects the organization and dimensionality of network activity (Fig. 8A). Our analysis reveals that in both homogeneous and heterogeneous networks, the firing rate variability is distributed across multiple PCs rather than being dominated by the first PC (PC1), which only accounts for less than 10% of the total variance (Fig. 8, A and B). This high-dimensional representation suggests that the network uses a rich set of activity patterns to encode the complex input signal, contributing to reliable and robust input representation.

Now, we examine trial-to-trial reliability in the projections into the subspace consisting of the three dominant components (PC1 to PC3). Both homogeneous and heterogeneous networks exhibit trial-to-trial stability in the projection onto PC1, reflecting the network-wide response to external input (Fig. 8, A and B). However, the homogeneous network exhibits considerable trial-to-trial variability in PC2 and PC3 (Fig. 8, A and C). In contrast, heterogeneous networks ($\sigma_{\tau_L} = 3$ and 8 ms) demonstrate stable structures of population responses across trials, indicating a reliable representation of the MG input signals in the subspace (Fig. 8, A and C). Actually, a higher degree of timescale diversity ($\sigma_{\tau_L} = 8$ ms) leads to more markedly reduced trial-to-trial variabilities in all components (Fig. 8C). Thus, heterogeneous networks achieve a stable high-dimensional structure in neural population response activities to represent the input in more details reliably.

The stable structure embedded in heterogeneous networks can be attributed to an input-driven transient dynamics, which enforces representation robustness. To demonstrate this, we introduced a random perturbation at an arbitrary time point and examined the three subsequent sections of the network's responses, focusing on the three dominant PCs (Fig. 9A).

During the immediate response to perturbation [section (a)], the manifold deviates substantially from that observed without perturbation (Fig. 9, A and B). However, in the subsequent sections (b) and (c), this deviation rapidly diminishes, indicating a quick convergence back to the input-driven trajectory (Fig. 9, A and B). This rapid convergence suggests the presence of an input-slaved trajectory (*26*).

The fast convergence also reflects the stability of performance in the MG series reconstruction task (Fig. 9C), indicating that the input-induced spatiotemporal modes are stable. Although timescale diversity increases the sensitivity of local sites, it still enhances the reliability of input signal representation because networks with input-induced DMD modes can settle into stable, input-induced activity patterns.

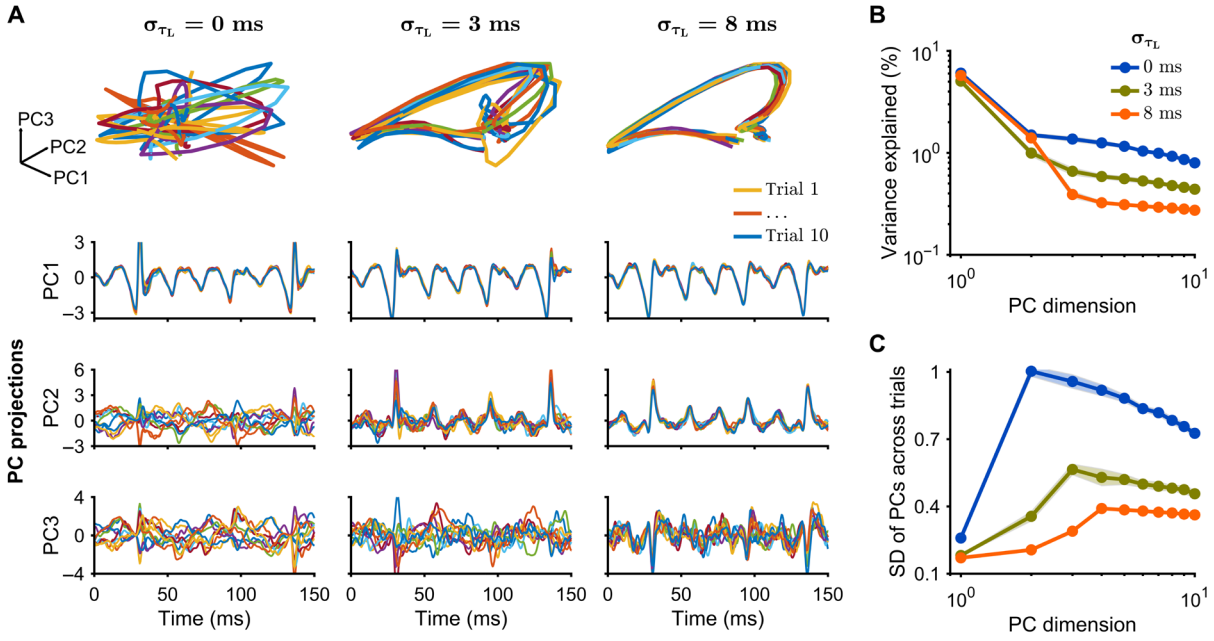

Fig. 8. PCA of the network activities under MG series input with $f_{MG} = 50$. (**A**) Projections of population responses into 3D space of PC1 to PC3 (top) at $\sigma_{\tau_L} = 0$ ms (left), 3 ms (middle), and 8 ms (right). The overlapped colored lines represent 10 repeated trials. (**B**) Percentages of variance explained by PCs. (**C**) Average trial-to-trial SDs of PCs calculated across 20 trials averaged over time.

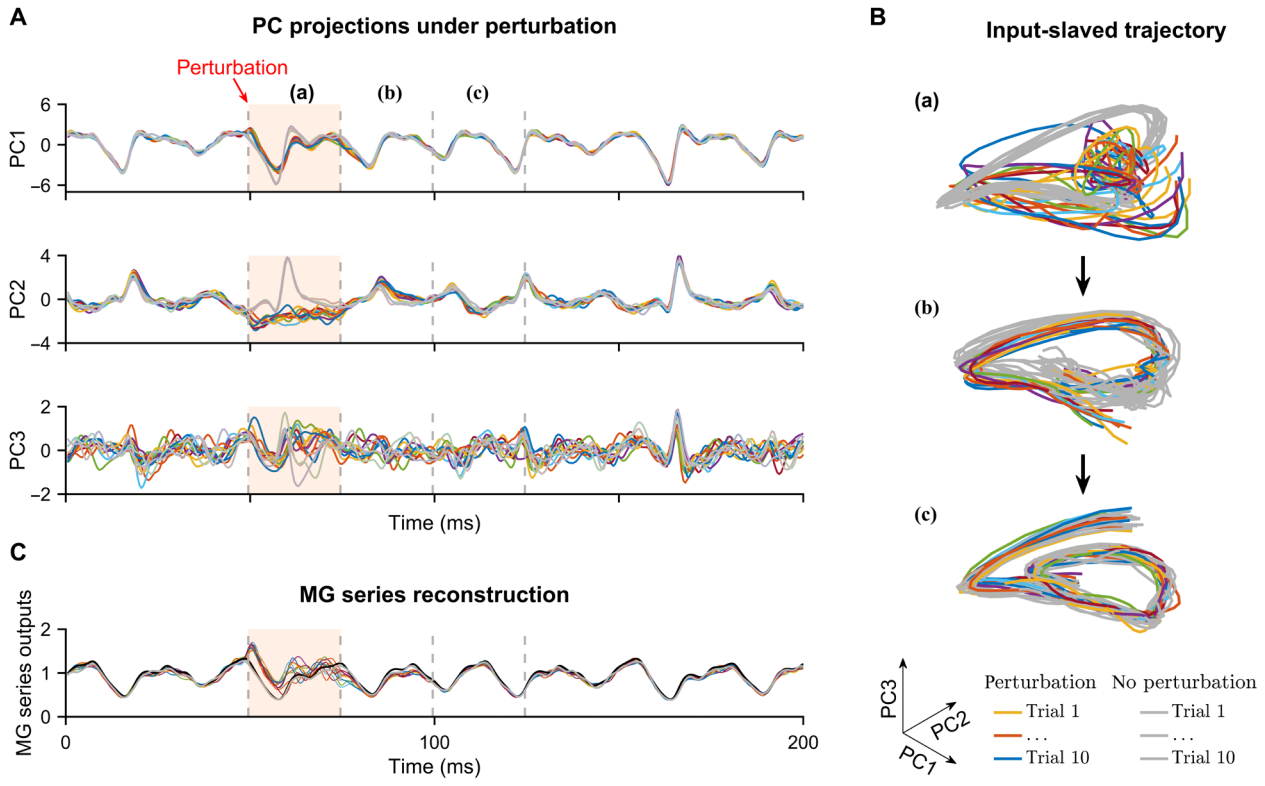

Fig. 9. Input-slaved trajectory of neural response under noise perturbation in the heterogeneous network (σ_{τ_L} = 8 ms). (**A**) Projections of noise-perturbed population responses into PC1, PC2, and PC3. Shaded regions (starting at 50 ms and lasting for 25 ms) indicate the period during which each neuron receives an independent Gaussian noise. (**B**) Projections of perturbed population responses into 3D space, where (a), (b), and (c) correspond to three distinct areas delineated by dashed lines in (A), representing the perturbation period and subsequent intervals. (**C**) MG series reconstructed from network responses to noise perturbation. In (A) to (C), the overlapping colored lines represent 10 repeated trials with noise perturbation, while gray lines represent trials without perturbation.

These results demonstrate that heterogeneous networks can generate input-slaved trajectories to robustly represent inputs, even when local activity is irregular, variable, and sensitive to perturbations. Therefore, we uncover the underlying dynamical mechanism that enables reliable neural representation and computation in the presence of neural heterogeneity.

Timescale diversity expanding representation space in the asynchronous state

Last, we demonstrate that the dynamical mechanism described above can also explain the robust role of timescale diversity in enhancing the reliability of representation in various σ_i / σ_e ratios (Fig. 4D) and in randomly shuffled networks (fig. S6). For our investigation, we consider the asynchronous state in a homogeneous or heterogeneous network with $\sigma_i / \sigma_e = 0.5$ as an example.

It is well known that balanced networks can respond linearly to inputs and closely track them (*10*, *34*). However, this responsiveness is limited to low-dimensional inputs, primarily 1D signals such as linear or sinusoidal input. This limitation arises because, in the asynchronous state, the network maintains a global E-I balance and a macroscopic steady state characterized by 1D dynamics, and neuronal firing rates are Gaussian distributed with low variability (similar to Fig. 2, F and G). The dynamics along other dimensions are highly stable and rarely react to input, as confirmed in our DMD analysis (fig. S10, A and B).

In contrast, with timescale diversity, neuronal firing rates are heterogeneously distributed, with a subset of neurons exhibiting low activity levels and high sensitivity to inputs. This enhanced responsiveness of local populations can disrupt the stability of dynamics in multiple dimensions. Consequently, the input can induce new modes (fig. S10B, right), allowing it to be tracked in a high-dimensional representation space (fig. S10, C and D). Therefore, timescale diversity effectively expands the representation space even in the asynchronous state, enabling the network to represent complex signals. Our framework thus captures its underlying dynamical mechanism.

Similar roles of other neural heterogeneities explained by the same dynamical mechanism

Various neural heterogeneities have contributed substantially to reliable neural computation (*13*, *16*, *17*, *21*, *22*). Our aim is to establish a general framework for understanding the roles of various forms of neural heterogeneity in reliable representation and computation. We now investigate whether the roles of other forms of neural heterogeneity can be explained by the same dynamical mechanism discussed earlier. As an illustration, we investigate the role of nonuniform input connections, characterized by the correlation range $\sigma_{W_{in}}$ of input weights. This parameter $\sigma_{W_{in}}$ regulates the spatial heterogeneity of the input weight distribution: A smaller $\sigma_{W_{in}}$ yields more localized and heterogeneous input connections, whereas a larger $\sigma_{W_{in}}$ tends toward uniform input connections (details in Materials and Methods). It has been shown to improve the representation and computation (*13*) (also presented in Fig. 10A), and it is robust against various connection range ratios σ_i / σ_e (data not shown).

Our identified dynamical mechanism can elucidate the role of this input connection heterogeneity: (i) Disruption of coherent spatiotemporal patterns: The heterogeneity disrupts the intrinsic coherent spatiotemporal patterns, inducing firing rate heterogeneity and increasing site sensitivities (fig. S11, A and D). This allows the network to respond to external stimuli and capture the features of the input signal effectively. (ii) Promotion of consistent stimulus representation: It promotes consistent stimulus representation by globally inducing input-related dynamical modes beyond the intrinsic modes (Fig. 10C). (iii) Input-slaved trajectories in an expanded representation space: It expands the representation space to higher dimensions, forming a high-dimensional input-slaved trajectory that reliably represents the input (Fig. 10, D and E).

As spike threshold heterogeneity and network in-degree heterogeneity also induce firing rate heterogeneity and enhance neuronal sensitivities with more highly sensitive neurons (fig. S11) (*16*, *22*), their effects on network dynamics and function can be accounted for by the same mechanism we have revealed, whereby variations in neuronal properties enhance computation's reliability (figs. S12 and S13). Thus, this mechanism may serve as a general framework for understanding the roles of various forms of neural heterogeneities in reliable representation and computation.

DISCUSSION

This study elucidates the dynamical mechanism underlying reliable representation and computation in SNNs with neural heterogeneity. We start by exploring the roles of two biologically plausible neuronal timescale diversities and demonstrate that neural heterogeneity disrupts intrinsic coherent spatiotemporal patterns (*13*, *25*), induces firing rate heterogeneity, enhances local responsive sensitivity, and aligns neural network activity closely with inputs. This process induces input-related dynamical modes, expands representation space, and forms high-dimensional input-slaved trajectories that reliably represent the input and ensure robust neural information processing against noise, despite neuronal spikings being variable over time and across repeated stimulation trials (*35*–*38*). Thus, we have uncovered a dynamical mechanism that reconciles inherent cortical variability

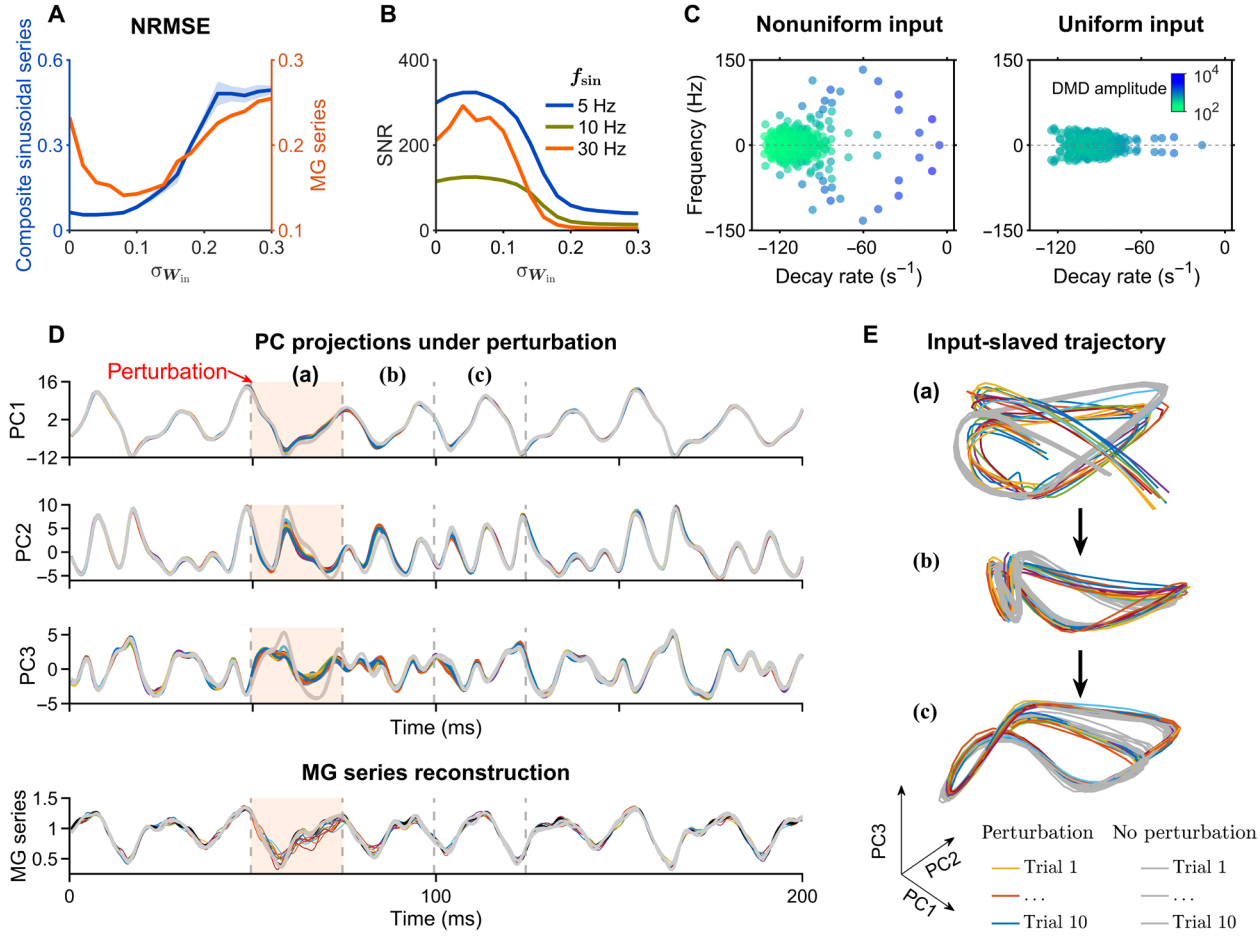

Fig. 10. Our mechanism explaining the role of nonuniform input connections in reliable computation. (**A**) NRMSE plotted against $\sigma_{W_{in}}$ for tasks of input-output mapping (blue line) and MG series reconstruction (orange line). (**B**) Averaged SNR plotted against $\sigma_{W_{in}}$ at f_{sin} = 5, 10, or 30 Hz. (**C**) DMD eigenvalue spectrum of neural responses in networks with nonuniform ($\sigma_{W_{in}}$ = 0.06, left) or uniform ($\sigma_{W_{in}}$ = 1, right) input connections. Dot colors represent mode amplitudes. (**D**) Top: Projections of noise-perturbed population responses into PC1, PC2, and PC3. Bottom: MG series reconstructed from network activities under random noise perturbation. (**E**) Perturbed population response in the PC1 to PC3 space. Panels (D) and (E) represent the network with nonuniform input connections ($\sigma_{W_{in}}$ = 0.06), where line colors and shaded regions denote the same as those in Fig. 9. Default time constants are τ_L = 20 ms and τ_Γ = 20 ms.

with reliable representation of external inputs. This mechanism also explains the similar roles of other neural heterogeneities, such as nonuniform input connections, spike threshold heterogeneity, and network in-degree heterogeneity, serving as a potentially general framework for understanding the role of various forms of neural heterogeneities in reliable representation and computation.

Roles of neural heterogeneity

Neural heterogeneity, which includes diversity in morphology, type, excitability, connectivity, ion channel distributions, and timescales, is ubiquitous in the brain (*18*–*20*). Neuron-to-neuron variability in molecular, genetic, and physiological features is increasingly recognized as a critical aspect of brain function. This biophysical diversity enriches the neural system's dynamical repertoire, fostering individual variability and complex neural dynamics. Complexity and heterogeneity are fundamental to neurobiological systems, manifesting at every level and process, and are intricately linked to the systems' emergent collective behaviors and functions. Numerous hypothetical roles of neural heterogeneity (*39*) have been suggested, including the following: (i) population coding: enhancing the neuron population's ability to encode information efficiently (*40*, *41*); (ii) reliability: increasing the reliability of neural computations (*13*, *42*); (iii) working memory: supporting complex cognitive functions (*43*–*45*) and functional specialization in neural computation (*24*); and (iv) reduction in pathological synchronization: preventing the onset of pathological states such as epilepsy (*22*, *46*).

Neural heterogeneity profoundly influences the functional repertoire and adaptability of neural circuits. Recent computational studies underscore the importance of spike threshold heterogeneity in enhancing neural network capabilities (*24*), such as efficient and robust encoding of stimuli (*16*, *47*, *48*), improving information transmission and learning (*49*), and maintaining robustness and persistence of brain function over time and in the face of changing environments (resilience) (*22*). On the other hand, neural heterogeneity of the membrane time constants of neurons makes learning complex tasks more stable and robust (*17*), indicating that this observed heterogeneity is a vital component of adaptive neural systems. Moreover, reservoir computing models equipped with diverse timescales outperform homogeneous models in both short- and long-term predictions of multiscale chaotic dynamics, illustrating the value of neural heterogeneity in optimizing temporal processing (*23*).

Despite these advancements, a comprehensive dynamical mechanism that unified the roles of various forms of neural heterogeneities and explains their contributions to reliable representation and computation remains to be established. Our study addresses this gap by first investigating the influence of timescale diversity on network dynamics (*50*) and its role in shaping reliable neural representation (*24*). Our findings highlight the substantial role of timescale diversity in reliable representation and computation, achieved by dissociating two key timescales: leakage time constant τ_L and responsive time constant τ_Γ (*18*, *24*), as their correlation deteriorates their individual contributions to the reliability. We further uncover the underlying dynamical mechanism: local responsive sensitivity and globally input-slaved transient dynamics, which can also account for the roles of other forms of neural heterogeneities: nonuniform input connections, spike threshold heterogeneity, and network in-degree heterogeneity. Thus, our study provides a cohesive framework that integrates diverse forms of heterogeneities, shedding light on the variability across multiple neuronal features, opening a new window and providing deeper insights into the role of neural heterogeneity, and potentially unifying the underlying dynamical mechanism for their roles in reliable representation and computation.

Input-slaved transient dynamics

The brain continuously receives and integrates vast amounts of environmental information, from sensory perception to task-driven behaviors and decision-making processes. Initial studies on neural encoding focused on individual neurons, revealing that certain neurons selectively respond to specific stimulus features such as spatial or temporal frequency, orientation, position, or depth, leading to sparse encoding. However, advancements in recording technologies have shifted research toward the collective dynamics of neural populations (*51*). The trajectories of these populations are typically constrained within low-dimensional manifolds in the high-dimensional space of neural activity (*9*), suggesting that the entire population dynamically encodes stimulus variables in a reduced or coarse-grained neural state space.

Robustness and reproducibility of sequential spatiotemporal responses are essential features of many neural circuits in the sensory and motor systems (*9*, *52*). Traditional dynamical regimes, such as fixed points, limit cycles, chaotic attractors, and continuous attractors, do not adequately describe reproducible transient sequential neural dynamics. Instead, a stable heteroclinic sequence (SHS) (*53*, *54*), although not an attractor, has been proposed to model these dynamics. SHS trajectories are highly sensitive to input but remain globally stable, with small deviations corrected by distributed stabilizing effects within the neural population. When the input is withdrawn, the system relaxes back to its baseline state. However, SHS is merely an illustrative model, requiring manual design rather than self-organization, and it lacks a solid biophysical basis. Besides, RNNs trained on cognitive tasks have shown that low-dimensional subspaces naturally emerge to support flexible computations at the population level (*55*, *56*). However, the internal connectivities of these artificial networks do not adhere to biological constraints such as Dale's principle, which states that neurons must be either excitatory or inhibitory.

Here, we found a self-organized dynamical mechanism to reliably and robustly produce such input-slaved trajectories for representing the input, based on biologically plausible E-I recurrent SNNs with neural heterogeneity. With no need for predesigned SHS-like dynamical structures (*57*), neural heterogeneity disrupts intrinsic coherence between neurons, rendering them sensitive to input for flexible computations. The formed trajectories are transient and nonstationary (Fig. 7C), entirely input induced, and embedded in the complex spatiotemporal neural activities. Despite its distributed coding of the input (Fig. 6C) and substantial variability of neuronal activities, neural heterogeneity effectively reduces the trial-to-trial variability of these trajectories in the noisy system. Thus, ubiquitous neuronal diversity provides a natural biophysical basis for reliable neural information processing.

Impacts on neuromorphic computing

Machine learning, particularly through artificial neural networks, has revolutionized computational applications across various fields by excelling in tasks such as regression, classification, prediction, and generation. However, optimizing these networks demands substantial computational resources and energy. Neuromorphic computing (*58*, *59*), which uses spiking potentials and waves instead of digital

bits, offers a promising alternative by leveraging the inherent efficiencies of biological systems. Recent advancements (*60*–*62*) have demonstrated the potential of using nonlinear waves, such as rogue waves and solitons, for neuromorphic computing. These waves' complex interactions make them particularly suitable for designing reservoir computing. By encoding information onto these waves, it is expected to substantially enhance the development of machine-learning devices leveraging wave dynamics.

Our study adds to this innovative field by elucidating the dynamical mechanism that underpins reliable representation and computation in biologically plausible SNNs characterized by neural heterogeneity. We found that neural heterogeneity disrupts coherent spatiotemporal patterns, thereby enhancing local sensitivity. This mechanism offers neurons liquid-like superior sensitivity, making them prone to capturing input information efficiently. It also renders the system to generate input-related dynamical modes that are intrinsically nonlinear waves (Fig. 7), thus expressing the complexity necessary for learning from a dataset.

This understanding of neural heterogeneity and its role in reliable computation provides a new avenue for designing reservoir computing models. By incorporating liquid wave reservoirs, one can leverage the benefits of neuromorphic computing while maintaining the complexity and efficiency needed for high-dimensional data representation and processing. Our discoveries, integrated with the principles of wave dynamics in neuromorphic computing, pave the way for developing advanced reservoir computing that leverages the efficiency and robustness of biological neural information processing.

Future work

Reliable representation is fundamental for subsequent neural processes such as memory, learning, and decision-making. In this study, basic E-I recurrent SNNs with neural diversity are used to investigate the underlying dynamical mechanisms of reliable representation and computation. This mechanism, characterized by local sensitivity and globally input-slaved transient dynamics due to neural heterogeneity, is expected to persist when the model incorporates more biological details, such as synaptic timescales and plasticity. Specifically, with synaptic timescales mediated by *N*-methyl-D-aspartate receptor currents, the input-slaved trajectories observed in our study can form the dynamical basis for transient memories, allowing for the temporary storage of information and its flexible use in decision-making (*63*–*65*). In addition, short-term plasticity can induce traces of hidden states essential for working memory (*66*–*70*). Therefore, our mechanism, which induces high-dimensional input-slaved trajectories, can serve as a substrate for working memory. We plan to investigate these issues further in the future.

MATERIALS AND METHODS

Network model

In this study, we use a spatially extended network of current-based LIF neurons ($N = 50{,}000$), with $N_e = 40{,}000$ excitatory ($\mathbf{e}$) and $N_i = 10{,}000$ inhibitory ($\mathbf{i}$) neurons uniformly spaced on a 2D sheet: $\Gamma = [0,1] \times [0,1]$, with torus-like periodic boundaries (Fig. 1A). For a neuron located at the coordinate (i,j) within population $\mathbf{a} \in \{\mathbf{e},\mathbf{i}\}$, its membrane potential $v^{\mathbf{a}}_{i,j}$ evolves as

$$C_{i,j}\frac{dv^{\mathbf{a}}_{i,j}(t)}{dt} = g_L^{i,j}\left[V_L - v^{\mathbf{a}}_{i,j}(t)\right] + g_\Gamma\left[\sum_{i'j'} K^{\mathbf{ab}}_{ij,i'j'}\sum_n \delta\left(t - t^n_{i'j'}\right) + F^{\mathbf{a}}_0 + F^{\mathrm{stim}}_{i,j}(t)\right] \quad (1)$$

where $V_L = -70$ mV is the resting potential, $C_{i,j}$ is the membrane capacitance, and $g_L^{i,j}$ is the leak conductance. The term g_Γ represents the network drive strength in the current-based synaptic model, capturing the effects of network activity, background input, and external stimuli. $F^{\mathrm{stim}}_{i,j}(t)$ denotes a time-varying external stimulus, while $F^{\mathbf{e}}_0 = 60$ mV and $F^{\mathbf{i}}_0 = 46$ mV denote constant background inputs for excitatory and inhibitory neurons, respectively. Here, $t^n_{i'j'}$ denotes the nth spike time of a neuron at coordinate (i',j') within population $\mathbf{b} \in \{\mathbf{e},\mathbf{i}\}$. When $v^{\mathbf{a}}_{i,j}(t)$ exceeds the spike threshold $V_{\mathrm{th}} = -50$ mV, the neuron at coordinate (i,j) emits a spike and then its membrane potential is reset to $V_{\mathrm{reset}} = -75$ mV for a refractory period of $\tau_{\mathrm{ref}} = 2$ ms.

To capture physiologically relevant distance-dependent connectivity patterns as observed in the mammalian cortex (*12*, *71*–*73*), we use a spatially extended network model (*13*, *27*). The synaptic strength from population $\mathbf{b}$ to $\mathbf{a}$ is defined as

$$K^{\mathbf{ab}}_{ij,i'j'} = \begin{cases} j_{\mathbf{ab}} & \text{with prob. } \bar{p}_{\mathbf{ab}}G(\mathbf{u};\sigma_{\mathbf{b}}) \\ 0 & \text{otherwise} \end{cases} \quad (2)$$

where $G(\mathbf{u};\sigma_{\mathbf{b}})$ is a 2D wrapped Gaussian function defining the connection probability based on the spatial distance $\mathbf{u} = (i-i', j-j')$ between neurons at coordinates (i,j) and (i',j'). The SD of the Gaussian function $\sigma_{\mathbf{b}}$ determines the spatial width of excitatory and inhibitory synaptic projections. Unless stated otherwise, we use the excitatory and inhibitory projection width: $\sigma_{\mathbf{e}} = 0.05$ and $\sigma_{\mathbf{i}} = 0.1$. The average connection probabilities for excitatory and inhibitory populations are $\bar{p}_{\mathbf{ee}} = \bar{p}_{\mathbf{ie}} = 0.0125$ and $\bar{p}_{\mathbf{ei}} = \bar{p}_{\mathbf{ii}} = 0.05$, with synaptic weights defined as $j_{\mathbf{ee}} = 2$ mV, $j_{\mathbf{ie}} = 4$ mV, and $j_{\mathbf{ei}} = j_{\mathbf{ii}} = -5$ mV.

To validate the robustness of our findings across diverse network structures, we constructed randomized networks by shuffling the connections within the spatial networks while preserving each neuron's original number of incoming and outgoing connections (its in-degree and out-degree distributions). In addition, we examined networks with heterogeneous in-degree connectivity, modeled as a lognormal distribution of the number of incoming connections to neurons, reflecting the experimentally observed diversity in input connectivity among cortical neurons (*74*). This distribution is given by the probability density function

$$f\left(k_{\mathrm{in}};\mu_{k_{\mathrm{in}}},\sigma_{k_{\mathrm{in}}}\right) = \frac{1}{k_{\mathrm{in}}\sigma_{k_{\mathrm{in}}}\sqrt{2\pi}}\exp\left[-\frac{\left(\ln k_{\mathrm{in}} - \mu_{k_{\mathrm{in}}}\right)^2}{2\sigma^2_{k_{\mathrm{in}}}}\right] \quad (3)$$

where k_{in} represents the in-degree of a neuron, $\mu_{k_{\mathrm{in}}} = 1000$ is the mean of the in-degree distribution, and $\sigma_{k_{\mathrm{in}}}$ controls the variance, with larger values corresponding to increased in-degree heterogeneity.

Timescale diversity and spike threshold diversity

Cortical neurons exhibit diversity in both morphological features and electrophysiological properties. Data-driven modeling based on the Allen Cell Types Database reveals a wide distribution of parameters, such as capacitance and conductance (*75*). In this study, we considered two distinct types of time constants contributing to timescale diversity within the LIF neuron model: the leakage time constant ($\tau_L^{i,j} = C_{i,j}/g_L^{i,j}$), which characterizes the timescale over which the membrane potential returns to resting in the absence of input, and the gain time constant ($\tau_\Gamma^{i,j} = C_{i,j}/g_\Gamma$), which indicates

the neuron's response gain to incoming stimuli, with its inverse representing this gain (Fig. 1C) (*18*, *24*).

Leakage timescale diversity arises from diverse membrane capacitance and conductance among neurons, while gain timescale diversity primarily reflects capacitance variability. To model the experimentally observed long-tail distributions of neuronal parameters (*18*), we used a lognormal distribution of neuronal timescales

$$f\left(\tau_m;\mu_{\tau_m},\sigma_{\tau_m}\right)=\frac{1}{\tau_m\sigma_{\tau_m}\sqrt{2\pi}}\exp\left[-\frac{\left(\ln\tau_m-\mu_{\tau_m}\right)^2}{2\sigma_{\tau_m}^2}\right] \quad (4)$$

Here, $m\in\{\mathrm{L},\Gamma,\mathrm{C}\}$, where these subscripts index the timescale types: L for leakage, Γ for gain, and C for common timescales. τ_m represents the general timescale parameter (whether leakage or gain), with μ_{τ_m} and σ_{τ_m} denoting the mean and SD of the timescale distribution. In our study, we set $\mu_{\tau_m}=20$ ms. σ_{τ_m} denotes the parameter controlling the degree of variability in the τ_L (or τ_Γ) distribution. Higher values of σ_{τ_m} represent a greater degree of timescale diversity.

Leakage and gain timescales may be correlated, with correlation parameter denoted as ρ. When τ_L equals τ_Γ ($\rho=1$), the model is equivalent to that used in the previous study, which used a single timescale parameter (*17*). In this study, we sampled τ_L and τ_Γ from a shared set τ_C to generate correlated distributions. Specifically, we randomly selected a proportion of $1-\rho$ from the independent distribution τ_L (or τ_Γ) and the remaining proportion ρ from a common distribution τ_C, resulting in independent timescales when $\rho=0$ and fully correlated timescales when $\rho=1$. In cases where τ_L and τ_Γ are correlated, we equated σ_{τ_L}, σ_{τ_Γ}, and σ_{τ_C}, denoting this shared timescale variability as $\sigma_{\tau_{\mathrm{L},\Gamma}}$ for consistency.

In addition, we considered other types of neural heterogeneities, such as spike threshold diversity, which was also modeled using a lognormal distribution

$$f\left(V_\mathrm{th};\overline{V_\mathrm{th}},\sigma_{V_\mathrm{th}}\right)=\frac{1}{V_\mathrm{th}\sigma_{V_\mathrm{th}}\sqrt{2\pi}}\exp\left[-\frac{\left(\ln V_\mathrm{th}-\overline{V_\mathrm{th}}\right)^2}{2\sigma_{V_\mathrm{th}}^2}\right] \quad (5)$$

where $\overline{V_\mathrm{th}}=-50$ mV is the mean spike threshold and the SD σ_{V_th} controls the degree of spike threshold diversity.

To measure firing rates, we used a coarse-graining approach by partitioning the 2D network into 2500 distinct sites, each comprising 16 adjacent excitatory and 4 inhibitory neurons. Neurons within each site share identical parameters, while across sites, neuronal properties and external inputs vary according to the preset heterogeneity.

External inputs

In this study, we examined the external time-varying input received by each neuron within the network. This input is defined as $F_{i,j}^{\mathrm{stim}}(t)=W_\mathrm{in}(i,j)I_\mathrm{stim}(t)$, where $W_\mathrm{in}(i,j)$ denotes the input weight of a neuron located at coordinate (i,j) and $I_\mathrm{stim}(t)$ represents the external driving signal.

We considered two types of input weight distributions: (i) uniform input connections, where $W_\mathrm{in}(i,j)$ is constant at 1, and (ii) nonuniform input connections, where the weight varies across sites. For the latter, we generated W_in such that input weights are similar for nearby neurons while varying spatially for more distant ones. This was achieved using spatially correlated Gaussian noise with a mean of zero and a covariance function expressed as

$$\mathrm{cov}\left[W_\mathrm{in}(\mathbf{x}),W_\mathrm{in}(\mathbf{x}+\mathbf{u})\right]=\exp\left(-\frac{|\mathbf{u}|^2}{2\sigma_{W_\mathrm{in}}^2}\right) \quad (6)$$

where $|\mathbf{u}|=|(i-i',j-j')|$ denotes the spatial distance. The parameter σ_{W_in} determines the spatial correlation range of W_in in the 2D space. The weight distribution of W_in becomes increasingly spatially heterogeneous as σ_{W_in} decreases.

Three types of time series were used as external driving signals: a periodic sinusoidal series, a chaotic MG series, and a Lorenz series. Among these, the MG signal exhibits a quasi-periodic spectral property, whereas the Lorenz system lacks apparent quasi-periodic spectral characteristics. The sinusoidal periodic series is mathematically defined as

$$I_\mathrm{sin}(t)=\epsilon\cdot\sin\left(2\pi f_\mathrm{sin}t\right) \quad (7)$$

where f_sin and ϵ represent the frequency and amplitude of the sinusoidal stimulus signal, respectively. The MG chaotic time series is represented as

$$I_\mathrm{MG}(t)=\epsilon\cdot U(t) \quad (8)$$

where the amplitude $\epsilon=20$ mV and the variable $U(t)$ is governed by the MG equation

$$\frac{dU(t)}{dt}=\frac{f_\mathrm{MG}}{20}\left[\frac{\alpha U\left(t-\tau_\mathrm{MG}\right)}{1+U\left(t-\tau_\mathrm{MG}\right)^\gamma}-\beta U(t)\right] \quad (9)$$

where the parameters $\alpha=0.2$, $\beta=0.1$, and $\gamma=10$ are dimensionless and define the system dynamics along with a time delay of $\tau_\mathrm{MG}=17$ ms. The parameter f_MG is pivotal in controlling the pace of the MG dynamics. A higher value of f_MG accelerates the evolution of the MG equation within a specified duration, thereby regulating the frequency of the quasi-periodic MG series.

The Lorenz-driven input $I_\mathrm{Lorenz}(t)$ is defined as

$$I_\mathrm{Lorenz}(t)=\epsilon\cdot L(t) \quad (10)$$

where $\epsilon=20$ mV represents the amplitude of the Lorenz stimulus signal and $L(t)$ denotes the first dimension of the Lorenz attractor data generated by the Lorenz system. In our simulation, $L(t)$ corresponds to $x(t)$, which is described by the following equations

$$\begin{cases}\dfrac{dx}{dt}=\sigma(y-x),\\ \dfrac{dy}{dt}=x(\rho-z)-y,\\ \dfrac{dz}{dt}=xy-\beta z\end{cases} \quad (11)$$

where the parameters are $\sigma=20$, $\rho=50$, and $\beta=\frac{8}{3}$.

Response robustness under noise perturbation

To examine the noise robustness of the network's response to external signal input, we applied independent Gaussian noise to the excitatory and inhibitory neurons within each of the 2500 sites: $F_{i,j}^{\mathrm{stim}}(t)=W_\mathrm{in}(i,j)\left[I_\mathrm{stim}(t)+I_\mathrm{noise}^{i,j}(t)\right]$. Neurons of the same type shared the same noise, while distinct types of neurons in each site received independent noise during a defined time period, described by

$$I_{\text{noise}}^{i,j}(t) = \epsilon \cdot \xi_{i,j}(t), \quad \text{for } t \in [t_0, t_0 + T] \tag{12}$$

Here, $\xi_{i,j}(t) \sim \mathcal{N}(0,1)$ is a standard Gaussian process with covariance: $\text{cov}\left[\xi_{i,j}(t), \xi_{i',j'}(t)\right] = \delta_{ij}$. The noise was applied for a duration $T = 25$ ms with an amplitude $\epsilon = 40$ mV.

Measurements

Instantaneous neural firing rate

In our study, we recorded coarse-grained neural firing rates $R(t)$ from 2500 sites across the whole network, with each recording site comprising $N_{\text{local}} = 16$ adjacent excitatory neurons. For each recording site, the site firing rate $R(t)$ was calculated as follows

$$R(t) = \frac{1}{N_{\text{local}} \cdot \delta T} \sum_{i=1}^{N_{\text{local}}} N_i(t, t + \delta T) \tag{13}$$

where $N_i(t, t+\delta T)$ represents the spike count of neuron i within a time bin of $\delta T = 0.5$ ms.

Synchrony index

To quantify the collective spiking synchronization of neurons within each recording site, we used the synchrony index based on the averaged Pearson correlation coefficient of spike counts between neuron pairs. The synchrony index is defined as follows

$$\text{synchrony index} = \left\langle \frac{\text{cov}\left[N_i(t, t+\Delta T), N_j(t, t+\Delta T)\right]}{\sqrt{\text{var}\left[N_i(t, t+\Delta T)\right]\text{var}\left[N_j(t, t+\Delta T)\right]}} \right\rangle \tag{14}$$

where $N_i(t, t+\Delta T)$ and $N_j(t, t+\Delta T)$ denote the spike counts of neurons i and j within a time window of $\Delta T = 100$ ms. Covariances (cov) and variances (var) of these spike counts were computed across the windows. The notation $\langle \cdot \rangle$ denotes averaging across all neuron pairs, excluding the cases where $i = j$.

Spectrum analysis and sensitivity

The power spectrum $S(f)$ of site firing rates was calculated using the fast Fourier transform, and the mean power spectrum was then derived by averaging the power spectra across all recording sites: $< S(f) >$.

The SNR was used to quantify the strength of the network's response to external periodic stimuli. On the basis of the power spectral density $S(f)$ of neural response activity, the SNR was calculated using the following equation

$$\text{SNR} = \frac{S(f_{\text{sin}}) - N(f_{\text{sin}})}{N(f_{\text{sin}})} \tag{15}$$

where $S(f_{\text{sin}})$ denotes the power at the frequency f_{sin} and $N(f_{\text{sin}})$ is the averaged power at nearby frequencies within a small range (~ 1 Hz) around f_{sin}. A high SNR value indicates a strong response of neural activity to the external periodic stimulus at the frequency f_{sin}.

To quantify the sensitivity of the network's response to periodic input, we applied a weak sinusoidal stimulus to the network at frequency f_{sin} with a range of input amplitude ϵ. The network's responsiveness to the sinusoidal stimulus was approximated by the SNR at f_{sin}. Specifically, the site-responsive sensitivity was defined as the rate of change of the square root of the SNR with respect to the amplitude

$$\text{sensitivity} = \frac{\delta\left(\sqrt{\text{SNR}}\right)}{\delta\epsilon} \tag{16}$$

Taking the square root of SNR yields an approximate linear relationship between $\sqrt{\text{SNR}}$ and stimulus amplitude, as observed in our simulations when ϵ remained below the saturation threshold. Sensitivity was then determined by applying a series of weak sinusoidal stimuli with varying amplitudes, fitting a linear relationship between $\sqrt{\text{SNR}}$ and ϵ, and taking the slope as the sensitivity measure. This procedure enabled systematic quantification of the network's responsiveness to incremental amplitude changes, with higher sensitivity values indicating enhanced amplification of weak external signals at frequency f_{sin}.

Least square method

In our study, we extracted coarse-grained neural firing rates X (with a recording site number $n = 2500$) from network response activities and used them to reconstruct or predict the output signal $\hat{\mathbf{y}} = W_{\text{out}}X$. The readout weight matrix W_{out} that minimizes the difference between the reconstructed output $\hat{\mathbf{y}}$ and the target (desired) signal $\mathbf{y}$ is obtained through the ridge LSM

$$\begin{aligned} W_{\text{out}} &= \text{argmin} \sum_t \|\hat{\mathbf{y}} - \mathbf{y}\|_2^2 + \eta \|W_{\text{out}}\|_2^2 \\ &= \left(XX^{\top} + \eta I\right)^{-1} X\mathbf{y} \end{aligned} \tag{17}$$

where $\|\cdot\|_2$ is the Frobenius norm, I is the matrix, and $\eta = 100$ is the regularization parameter that penalizes large values in the parameter vector W_{out}. We explored the range of η from 0 to 200, finding that it does not substantially affect the main results of our study.

Dynamic mode decomposition

We used the DMD algorithm, a data-driven eigendecomposition method, to analyze the spatiotemporal pattern of network activity. DMD approximates the observed system dynamics directly from high-dimensional time-series data, allowing for the extraction of a low-dimensional representation of complex dynamics. By decomposing these dynamics into coherent spatiotemporal modes, DMD offers insights into underlying patterns and system behavior (*33*, *76*). The DMD procedure constructs a locally linear dynamical system proxy A

$$X' = AX, \qquad A \in \mathbb{R}^{n \times n} \tag{18}$$

X and X' are matrices containing snapshots of the network's state over time, where each column represents the network state vector at a specific time step.

$$X = \begin{bmatrix} | & | & & | \\ \boldsymbol{x}_1 & \boldsymbol{x}_2 & \cdots & \boldsymbol{x}_{t-1} \\ | & | & & | \end{bmatrix}, \quad X' = \begin{bmatrix} | & | & & | \\ \boldsymbol{x}_2 & \boldsymbol{x}_3 & \cdots & \boldsymbol{x}_t \\ | & | & & | \end{bmatrix} \in \mathbb{R}^{n \times (t-1)} \tag{19}$$

$\boldsymbol{x}_t \in \mathbb{R}^n$ represents the network state vector of coarse-grained neural firing rates at time t, where $n = 2500$ is the number of recording sites.

The optimal linear operator A is determined by minimizing the Frobenius norm error $\|X' - AX\|_{\text{F}}$. In practical application, the DMD algorithm to compute A and extract dynamic modes involves these key steps (*76*):

1) Decompose X using singular value decomposition: $X \approx U_r \Sigma_r V_r^T$, where $U_r \in \mathbb{R}^{n\times r}$ and $V_r^T \in \mathbb{R}^{r\times t}$ contain the left and right singular vectors, respectively. $\Sigma_r \in \mathbb{R}^{r\times r}$ is a diagonal matrix of the largest r singular values. Here, r represents the truncated rank, retaining the dominant singular values to capture essential dynamics.

2) Project the full matrix A onto the proper orthogonal decomposition (POD) space to get the reduced dimensionality approximation of A within the POD basis: $\tilde{A} = U_r^T X' V_r \Sigma_r^{-1}$.

3) Calculate the rescaled operator, $\widehat{A} = \Sigma_r^{-1/2} \tilde{A} \Sigma_r^{1/2}$, and perform eigendecomposition, $\widehat{A} = Q \Lambda Q^T$, where Q and Λ are the eigenvector and diagonalizable eigenvalue matrices, respectively.

4) Calculate DMD modes as $\Phi = X' V_r \Sigma_r^{-1/2} Q$, where $\Phi \in \mathbb{R}^{n\times r}$ provides the spatial structures of the modes in the original high-dimensional space, with mode amplitudes given by $\mathrm{diag}\left(\Phi^T \Phi\right)$.

5) Use the DMD modes and eigenvalues to approximate future states of the system as $\widehat{X} = \Phi \Lambda^{t-1} Z = \sum_{k\in\mathbf{m}} \phi_k \lambda_k^{t-1} Z_k$, where $Z = \Phi^{\dagger} X_0$, with X_0 representing the initial system state and $\dagger$ denoting the pseudo-inverse. $\mathbf{m} = \{1, 2, \cdots, r\}$ is the set of selected DMD mode labels. ϕ_k and λ_k represent individual DMD modes and their corresponding eigenvalues.

In this study, we calculated the DMD operator A from network activity and selected DMD modes to predict the system's short-term future state. Using LSM, we reconstructed the target stimulus series from the predicted state $\widehat{X}$, where reconstruction accuracy reflects which DMD modes best capture the dynamic features of the stimuli. Essentially, DMD modes that accurately reconstruct the stimuli indicate high network responsivity to the input signal.

Reliability of neural representation

The reliability of the neural representation under external stimuli was quantified using the NRMSE in the test dataset

$$\mathrm{NRMSE} = \sqrt{\frac{\sum_{t=1}^{T} \|\widehat{\mathbf{y}}(t) - \mathbf{y}(t)\|_2^2}{T \cdot \mathrm{var}\left[\mathbf{y}(t)\right]}} \tag{20}$$

where T is the number of time steps and $\mathrm{var}\left[\mathbf{y}(t)\right]$ denotes the variance of the target signal. A low NRMSE value indicates a robust alignment between the reconstructed signal and the target sequence across multiple trials of repeated stimuli, reflecting consistent neural representations achieved by the network. Thus, a lower NRMSE value indicates higher reliability in the network representation. Here, the training and testing datasets consist of 50 and 10 trials of neural response data, respectively, with each trial lasting for a 500-ms stimulation duration.

Computer simulations

For numerical integration of the equations, we used the Euler method, except for the MG equation and Lorenz system, which required the fourth-order Runge-Kutta method for improved accuracy. The simulation time step was set to $dt = 0.05$ ms. To ensure statistically reliable results, we performed 20 independent simulations for each configuration. All simulations discarded data from the first 500 ms; each simulation lasted for 30 s. Specifically, for the SNR calculation, simulations were extended to 60 s, while for the calculation of spike count correlation, simulations lasted for 200 s.

Supplementary Materials

This PDF file includes:

Note S1
Figs. S1 to S13

REFERENCES AND NOTES

1. M. Tsodyks, T. Kenet, A. Grinvald, A. Arieli, Linking spontaneous activity of single cortical neurons and the underlying functional architecture. *Science* **286**, 1943–1946 (1999).
2. A. Renart, C. K. Machens, Variability in neural activity and behavior. *Curr. Opin. Neurobiol.* **25**, 211–220 (2014).
3. Y. Ziv, L. D. Burns, E. D. Cocker, E. O. Hamel, K. K. Ghosh, L. J. Kitch, A. El Gamal, M. J. Schnitzer, Long-term dynamics of CA1 hippocampal place codes. *Nat. Neurosci.* **16**, 264–266 (2013).
4. C. Stringer, M. Pachitariu, N. Steinmetz, C. B. Reddy, M. Carandini, K. D. Harris, Spontaneous behaviors drive multidimensional, brainwide activity. *Science* **364**, 255 (2019).
5. W. G. Gonzalez, H. Zhang, A. Harutyunyan, C. Lois, Persistence of neuronal representations through time and damage in the hippocampus. *Science* **365**, 821–825 (2019).
6. S. Ebrahimi, J. Lecoq, O. Rumyantsev, T. Tasci, Y. Zhang, C. Irimia, J. Li, S. Ganguli, M. J. Schnitzer, Emergent reliability in sensory cortical coding and inter-area communication. *Nature* **605**, 713–721 (2022).
7. M. M. Churchland, B. M. Yu, J. P. Cunningham, L. P. Sugrue, M. R. Cohen, G. S. Corrado, W. T. Newsome, A. M. Clark, P. Hosseini, B. B. Scott, D. C. Bradley, M. A. Smith, A. Kohn, J. A. Movshon, K. M. Armstrong, T. Moore, S. W. Chang, L. H. Snyder, S. G. Lisberger, N. J. Priebe, I. M. Finn, D. Ferster, S. I. Ryu, G. Santhanam, M. Sahani, K. V. Shenoy, Stimulus onset quenches neural variability: A widespread cortical phenomenon. *Nat. Neurosci.* **13**, 369–378 (2010).
8. R. Laje, D. V. Buonomano, Robust timing and motor patterns by taming chaos in recurrent neural networks. *Nat. Neurosci.* **16**, 925–933 (2013).
9. J. A. Michaels, B. Dann, H. Scherberger, Neural population dynamics during reaching are better explained by a dynamical system than representational tuning. *PLOS Comput. Biol.* **12**, e1005175 (2016).
10. C. van Vreeswijk, H. Sompolinsky, Chaos in neuronal networks with balanced excitatory and inhibitory activity. *Science* **274**, 1724–1726 (1996).
11. A. Renart, J. De La Rocha, P. Bartho, L. Hollender, N. Parga, A. Reyes, K. D. Harris, The asynchronous state in cortical circuits. *Science* **327**, 587–590 (2010).
12. R. B. Levy, A. D. Reyes, Spatial profile of excitatory and inhibitory synaptic connectivity in mouse primary auditory cortex. *J. Neurosci.* **32**, 5609–5619 (2012).
13. R. Pyle, R. Rosenbaum, Spatiotemporal dynamics and reliable computations in recurrent spiking neural networks. *Phys. Rev. Lett.* **118**, 018103 (2017).
14. M. R. Ricard, S. Mischler, Turing instabilities at hopf bifurcation. *J. Nonlinear Sci.* **19**, 467–496 (2009).
15. W. Maass, T. Natschläger, H. Markram, Real-time computing without stable states: A new framework for neural computation based on perturbations. *Neural Comput.* **14**, 2531–2560 (2002).
16. R. Gast, S. A. Solla, A. Kennedy, Neural heterogeneity controls computations in spiking neural networks. *Proc. Natl. Acad. Sci. U.S.A.* **121**, e2311885121 (2024).
17. N. Perez-Nieves, V. C. H. Leung, P. L. Dragotti, D. F. M. Goodman, Neural heterogeneity promotes robust learning. *Nat. Commun.* **12**, 5791 (2021).
18. Y. N. Billeh, B. Cai, S. L. Gratiy, K. Dai, R. Iyer, N. W. Gouwens, R. Abbasi-Asl, X. Jia, J. H. Siegle, S. R. Olsen, C. Koch, S. Mihalas, A. Arkhipov, Systematic integration of structural and functional data into multi-scale models of mouse primary visual cortex. *Neuron* **106**, 388–403.e18 (2020).
19. E. S. Lein, M. J. Hawrylycz, N. Ao, M. Ayres, A. Bensinger, A. Bernard, A. F. Boe, M. S. Boguski, K. S. Brockway, E. J. Byrnes, L. Chen, L. Chen, T.-M. Chen, M. C. Chin, J. Chong, B. E. Crook, A. Czaplinska, C. N. Dang, S. Datta, N. R. Dee, A. L. Desaki, T. Desta, E. Diep, T. A. Dolbeare, M. J. Donelan, H.-W. Dong, J. G. Dougherty, B. J. Duncan, A. J. Ebbert, G. Eichele, L. K. Estin, C. Faber, B. A. Facer, R. Fields, S. R. Fischer, T. P. Fliss, C. Frensley, S. N. Gates, K. J. Glattfelder, K. R. Halverson, M. R. Hart, J. G. Hohmann, M. P. Howell, D. P. Jeung, R. A. Johnson, P. T. Karr, R. Kawal, J. M. Kidney, R. H. Knapik, C. L. Kuan, J. H. Lake, A. R. Laramee, K. D. Larsen, C. Lau, T. A. Lemon, A. J. Liang, Y. Liu, L. T. Luong, J. Michaels, J. J. Morgan, R. J. Morgan, M. T. Mortrud, N. F. Mosqueda, L. L. Ng, R. Ng, G. J. Orta, C. C. Overly, T. H. Pak, S. E. Parry, S. D. Pathak, O. C. Pearson, R. B. Puchalski, Z. L. Riley, H. R. Rockett, S. A. Rowland, J. J. Royall, M. J. Ruiz, N. R. Sarno, K. Schaffnit, N. V. Shapovalova, T. Sivisay, C. R. Slaughterbeck, S. C. Smith, K. A. Smith, B. I. Smith, A. J. Sodt, N. N. Stewart, K.-R. Stumpf, S. M. Sunkin, M. Sutram, A. Tam, C. D. Teemer, C. Thaller, C. L. Thompson, L. R. Varnam, A. Visel, R. M. Whitlock, P. E. Wohnoutka, C. K. Wolkey, V. Y. Wong, M. Wood, M. B. Yaylaoglu, R. C. Young, B. L. Youngstrom, X. F. Yuan,

B. Zhang, T. A. Zwingman, A. R. Jones, Genome-wide atlas of gene expression in the adult mouse brain. *Nature* **445**, 168–176 (2007).
20. M. J. Hawrylycz, E. S. Lein, A. L. Guillozet-Bongaarts, E. H. Shen, L. Ng, J. A. Miller, L. N. van de Lagemaat, K. A. Smith, A. Ebbert, Z. L. Riley, C. Abajian, C. F. Beckmann, A. Bernard, D. Bertagnolli, A. F. Boe, P. M. Cartagena, M. M. Chakravarty, M. Chapin, J. Chong, R. A. Dalley, B. D. Daly, C. Dang, S. Datta, N. Dee, T. A. Dolbeare, V. Faber, D. Feng, D. R. Fowler, J. Goldy, B. W. Gregor, Z. Haradon, D. R. Haynor, J. G. Hohmann, S. Horvath, R. E. Howard, A. Jeromin, J. M. Jochim, M. Kinnunen, C. Lau, E. T. Lazarz, C. Lee, T. A. Lemon, L. Li, Y. Li, J. A. Morris, C. C. Overly, P. D. Parker, S. E. Parry, M. Reding, J. J. Royall, J. Schulkin, P. A. Sequeira, C. R. Slaughterbeck, S. C. Smith, A. J. Sodt, S. M. Sunkin, B. E. Swanson, M. P. Vawter, D. Williams, P. Wohnoutka, H. R. Zielke, D. H. Geschwind, P. R. Hof, S. M. Smith, C. Koch, S. G. N. Grant, A. R. Jones, An anatomically comprehensive atlas of the adult human brain transcriptome. *Nature* **489**, 391–399 (2012).
21. G. Chen, F. Scherr, W. Maass, A data-based large-scale model for primary visual cortex enables brain-like robust and versatile visual processing. *Sci. Adv.* **8**, eabq7592 (2022).
22. A. Hutt, S. Rich, T. A. Valiante, J. Lefebvre, Intrinsic neural diversity quenches the dynamic volatility of neural networks. *Proc. Natl. Acad. Sci. U.S.A.* **120**, e2218841120 (2023).
23. G. Tanaka, T. Matsumori, H. Yoshida, K. Aihara, Reservoir computing with diverse timescales for prediction of multiscale dynamics. *Phys. Rev. Res.* **4**, L032014 (2022).
24. R. Duarte, A. Morrison, Leveraging heterogeneity for neural computation with fading memory in layer 2/3 cortical microcircuits. *PLOS Comput. Biol.* **15**, e1006781 (2019).
25. E. Hunsberger, M. Scott, C. Eliasmith, The competing benefits of noise and heterogeneity in neural coding. *Neural Comput.* **26**, 1600–1623 (2014).
26. M. Shelley, D. McLaughlin, R. Shapley, J. Wielaard, States of high conductance in a large-scale model of the visual cortex. *J. Comput. Neurosci.* **13**, 93–109 (2002).
27. R. Rosenbaum, B. Doiron, Balanced networks of spiking neurons with spatially dependent recurrent connections. *Phys. Rev. X* **4**, 021039 (2014).
28. S. De Monte, F. d'Ovidio, E. Mosekilde, Coherent regimes of globally coupled dynamical systems. *Phys. Rev. Lett.* **90**, 054102 (2003).
29. W. Zou, M. Zhan, J. Kurths, Amplitude death in globally coupled oscillators with time-scale diversity. *Phys. Rev. E* **98**, 062209 (2018).
30. W. Zou, S. He, D. V. Senthilkumar, J. Kurths, Solvable dynamics of coupled high-dimensional generalized limit-cycle oscillators. *Phys. Rev. Lett.* **130**, 107202 (2023).
31. D. H. O'Connor, S. P. Peron, D. Huber, K. Svoboda, Neural activity in barrel cortex underlying vibrissa-based object localization in mice. *Neuron* **67**, 1048–1061 (2010).
32. M. C. Mackey, L. Glass, Oscillation and chaos in physiological control systems. *Science* **197**, 287–289 (1977).
33. P. J. Schmid, Dynamic mode decomposition of numerical and experimental data. *J. Fluid Mech.* **656**, 5–28 (2010).
34. C. van Vreeswijk, H. Sompolinsky, Chaotic balanced state in a model of cortical circuits. *Neural Comput.* **10**, 1321–1371 (1998).
35. M. N. Shadlen, W. T. Newsome, The variable discharge of cortical neurons: Implications for connectivity, computation, and information coding. *J. Neurosci.* **18**, 3870–3896 (1998).
36. D. Lee, N. L. Port, W. Kruse, A. P. Georgopoulos, Variability and correlated noise in the discharge of neurons in motor and parietal areas of the primate cortex. *J. Neurosci.* **18**, 1161–1170 (1998).
37. M. V. Sanchez-Vives, M. Mattia, A. Compte, M. Perez-Zabalza, M. Winograd, V. F. Descalzo, R. Reig, Inhibitory modulation of cortical up states. *J. Neurophysiol.* **104**, 1314–1324 (2010).
38. K. Cohen-Kashi Malina, B. Mohar, A. N. Rappaport, I. Lampl, Local and thalamic origins of correlated ongoing and sensory-evoked cortical activities. *Nat. Commun.* **7**, 12740 (2016).
39. J. Gjorgjieva, G. Drion, E. Marder, Computational implications of biophysical diversity and multiple timescales in neurons and synapses for circuit performance. *Curr. Opin. Neurobiol.* **37**, 44–52 (2016).
40. K. Padmanabhan, N. N. Urban, Intrinsic biophysical diversity decorrelates neuronal firing while increasing information content. *Nat. Neurosci.* **13**, 1276–1282 (2010).
41. S. J. Tripathy, K. Padmanabhan, R. C. Gerkin, N. N. Urban, Intermediate intrinsic diversity enhances neural population coding. *Proc. Natl. Acad. Sci. U.S.A.* **110**, 8248–8253 (2013).
42. J. Lengler, F. Jug, A. Steger, Reliable neuronal systems: The importance of heterogeneity. *PLOS ONE* **8**, e80694 (2013).
43. A. Renart, P. Song, X.-J. Wang, Robust spatial working memory through homeostatic synaptic scaling in heterogeneous cortical networks. *Neuron* **38**, 473–485 (2003).
44. Z. P. Kilpatrick, B. Ermentrout, B. Doiron, Optimizing working memory with heterogeneity of recurrent cortical excitation. *J. Neurosci.* **33**, 18999–19011 (2013).
45. J. Hass, S. Ardid, J. Sherfey, N. Kopell, Constraints on persistent activity in a biologically detailed network model of the prefrontal cortex with heterogeneities. *Prog. Neurobiol.* **215**, 102287 (2022).
46. S. Rich, H. M. Chameh, J. Lefebvre, T. A. Valiante, Loss of neuronal heterogeneity in epileptogenic human tissue impairs network resilience to sudden changes in synchrony. *Cell Rep.* **39**, 110863 (2022).
47. J. F. Mejias, A. Longtin, Optimal heterogeneity for coding in spiking neural networks. *Phys. Rev. Lett.* **108**, 228102 (2012).
48. F. Zeldenrust, B. Gutkin, S. Denéve, Efficient and robust coding in heterogeneous recurrent networks. *PLOS Comput. Biol.* **17**, e1008673 (2021).
49. G. Marsat, L. Maler, Neural heterogeneity and efficient population codes for communication signals. *J. Neurophysiol.* **104**, 2543–2555 (2010).
50. M. Y. Yim, A. Aertsen, S. Rotter, Impact of intrinsic biophysical diversity on the activity of spiking neurons. *Phys. Rev. E* **87**, 032710 (2013).
51. C. Stringer, M. Pachitariu, N. Steinmetz, M. Carandini, K. D. Harris, High-dimensional geometry of population responses in visual cortex. *Nature* **571**, 361–365 (2019)).
52. O. Mazor, G. Laurent, Transient dynamics versus fixed points in odor representations by locust antennal lobe projection neurons. *Neuron* **48**, 661–673 (2005).
53. M. Rabinovich, A. Volkovskii, P. Lecanda, R. Huerta, H. D. I. Abarbanel, G. Laurent, Dynamical encoding by networks of competing neuron groups: Winnerless competition. *Phys. Rev. Lett.* **87**, 068102 (2001).
54. M. Rabinovich, R. Huerta, G. Laurent, Transient dynamics for neural processing. *Science* **321**, 48–50 (2008).
55. A. Dubreuil, A. Valente, M. Beiran, F. Mastrogiuseppe, S. Ostojic, The role of population structure in computations through neural dynamics. *Nat. Neurosci.* **25**, 783–794 (2022).
56. M. Beiran, N. Meirhaeghe, H. Sohn, M. Jazayeri, S. Ostojic, Parametric control of flexible timing through low-dimensional neural manifolds. *Neuron* **111**, 739–753.e8 (2023).
57. M. I. Rabinovich, P. Varona, A. I. Selverston, H. D. I. Abarbanel, Dynamical principles in neuroscience. *Rev. Mod. Phys.* **78**, 1213–1265 (2006).
58. D. Ham, H. Park, S. Hwang, K. Kim, Neuromorphic electronics based on copying and pasting the brain. *Nat. Electron.* **4**, 635–644 (2021).
59. N. Farmakidis, B. Dong, H. Bhaskaran, Integrated photonic neuromorphic computing: Opportunities and challenges. *Nat. Rev. Electr. Eng.* **1**, 358–373 (2024).
60. T. W. Hughes, I. A. D. Williamson, M. Minkov, S. Fan, Wave physics as an analog recurrent neural network. *Sci. Adv.* **5**, eaay6946 (2019).
61. G. Marcucci, D. Pierangeli, C. Conti, Theory of neuromorphic computing by waves: Machine learning by rogue waves, dispersive shocks, and solitons. *Phys. Rev. Lett.* **125**, 093901 (2020).
62. H. Wang, H. Jianqi, A. Morandi, A. Nardi, F. Xia, X. Li, R. Savo, Q. Liu, R. Grange, S. Gigan, Large-scale photonic computing with nonlinear disordered media. *Nat. Comput. Sci.* , 429–439 (2024).
63. M. Lundqvist, P. Herman, E. K. Miller, Working memory: Delay activity, yes! Persistent activity? Maybe not. *J. Neurosci.* **38**, 7013–7019 (2018).
64. S. Zhou, M. Seay, J. Taxidis, P. Golshani, D. V. Buonomano, Multiplexing working memory and time in the trajectories of neural networks. *Nat. Hum. Behav.* **7**, 1170–1184 (2023).
65. D. V. Buonomano, G. Buzsáki, L. Davachi, A. C. Nobre, Time for memories. *J. Neurosci.* **43**, 7565–7574 (2023).
66. G. Mongillo, O. Barak, M. Tsodyks, Synaptic theory of working memory. *Science* **319**, 1543–1546 (2008).
67. M. G. Stokes, 'Activity-silent' working memory in prefrontal cortex: A dynamic coding framework. *Trends Cogn. Sci.* **19**, 394–405 (2015).
68. L. Kozachkov, J. Tauber, M. Lundqvist, S. L. Brincat, J.-J. Slotine, E. K. Miller, Robust and brain-like working memory through short-term synaptic plasticity. *PLOS Comput. Biol.* **18**, e1010776 (2022).
69. P. M. Bays, S. Schneegans, W. J. Ma, T. F. Brady, Representation and computation in visual working memory. *Nat. Hum. Behav.* **8**, 1016–1034 (2024).
70. D. G. Clark, L. F. Abbott, Theory of coupled neuronal-synaptic dynamics. *Phys. Rev. X* **14**, 021001 (2024).
71. D. Kätzel, B. V. Zemelman, C. Buetfering, M. Wölfel, G. Miesenböck, The columnar and laminar organization of inhibitory connections to neocortical excitatory cells. *Nat. Neurosci.* **14**, 100–107 (2011).
72. S. C. Seeman, L. Campagnola, P. A. Davoudian, A. Hoggarth, T. A. Hage, A. Bosma-Moody, C. A. Baker, J. H. Lee, S. Mihalas, C. Teeter, A. L. Ko, J. G. Ojemann, R. P. Gwinn, D. L. Silbergeld, C. Cobbs, J. Phillips, E. Lein, G. Murphy, C. Koch, H. Zeng, T. Jarsky, Sparse recurrent excitatory connectivity in the microcircuit of the adult mouse and human cortex. *eLife* **7**, e37349 (2018).
73. T. A. Hage, A. Bosma-Moody, C. A. Baker, M. B. Kratz, L. Campagnola, T. Jarsky, H. Zeng, G. J. Murphy, Synaptic connectivity to L2/3 of primary visual cortex measured by two-photon optogenetic stimulation. *eLife* **11**, e71103 (2022).
74. M. Okun, N. A. Steinmetz, L. Cossell, M. F. Iacaruso, H. Ko, P. Barthó, T. Moore, S. B. Hofer, T. D. Mrsic-Flogel, M. Carandini, K. D. Harris, Diverse coupling of neurons to populations in sensory cortex. *Nature* **521**, 511–515 (2015).
75. C. Teeter, R. Iyer, V. Menon, N. Gouwens, D. Feng, J. Berg, A. Szafer, N. Cain, H. Zeng, M. Hawrylycz, C. Koch, S. Mihalas, Generalized leaky integrate-and-fire models classify multiple neuron types. *Nat. Commun.* **9**, 709 (2018).
76. J. N. Kutz, S. L. Brunton, B. W. Brunton, J. L. Proctor, *Dynamic Mode Decomposition: Data-Driven Modeling of Complex Systems* (Society for Industrial and Applied Mathematics, 2016).

Acknowledgments: We thank W. Zou and C. Yao for discussions and Z. Wang for proofreading. **Funding:** This work is supported partly by the National Science Foundation of China under grant no. 12175242 (to D.Y.), the Natural Science Foundation of Zhejiang Province under grant no. LZ24A050007 (to D.Y.), and the Research Initiation Project of Zhejiang Lab under grant no. K2022KI0PI01 (to D.Y.). **Author contributions:** Conceptualization: S. Wu, S. Wang, G.C., C.Z., and D.Y. Methodology: S. Wu, G.C., H.H., and D.Y. Investigation: S. Wu and D.Y. Visualization: S. Wu, H.H., G.C., and D.Y. Supervision: H.H. and D.Y. Writing—original draft: S. Wu, G.C., and D.Y. Writing—review and editing: S. Wu, H.H., S. Wang, G.C., C.Z., and D.Y. Resources: S. Wu, H.H., and D.Y. Data curation: S. Wu, G.C., and D.Y. Validation: S. Wu, H.H., G.C., and D.Y. Formal analysis: S. Wu. Software: S. Wu. Project administration: H.H. and D.Y. Funding acquisition: D.Y. **Competing interests:** The authors declare that they have no competing interests. **Data and materials availability:** All data needed to evaluate the conclusions in the paper are present in the paper and/or the Supplementary Materials. Computer code for all simulations and analysis of the resulting data is available at https://doi.org/10.5281/zenodo.14054851.

Submitted 30 June 2024
Accepted 26 February 2025
Published 2 April 2025
10.1126/sciadv.adr3903